nature portfolio

https://doi.org/10.1038/s41586-022-04874-z

Supplementary information

Electrocatalytic metal hydride generation using CPET mediators

Supplementary Information for

Electrocatalytic metal hydride generation using CPET mediators

*Subal Dey, Fabio Masero, Enzo Brack, Marc Fontecave, Victor Mougel**

Correspondence to: mougel@inorg.chem.ethz.ch

Contents

Supplementary Data and Discussion

1. General Considerations

All experiments were performed under dry and argon atmosphere using either Schlenk techniques or gloveboxes (Vigor) equipped with a purifier unit. Water and oxygen levels were always kept below 1 ppm. Acetonitrile (CH_3CN), diethyl ether (Et_2O), THF and ethanol (EtOH) were purified on double alumina columns using an MBRAUN SPS-800 or Vigor solvent purification system. Et_2O and THF were vacuum distilled from K/benzophenone. Ethanol (EtOH) and methanol (MeOH) were dried over Mg turnings and distilled. All the solvents were degassed by three consecutive freeze-pump-thaw cycles. CH_3CN and MeOH were stored over activated 3 Å molecular sieves whereas all other solvents were stored over activated 4 Å molecular sieves. Water used for experiments was collected from a Thermo Scientific Gene Pure Pro UV US water purification system (18.2 $M\Omega\ cm^{-1}$). Ar and CO_2 used in electrochemical experiments were purified to ppb level of trace impurities using ZPure PolyGas I or Gatekeeper GPU S700DZ purifiers respectively. ^1H-NMR spectra were recorded on a Bruker Avance-III 300 MHz and Cryo-Probe Bruker Avance III 500 MHz spectrometers. NMR spectra were analysed and processed using MestReNova 12.0.3. FTIR spectroscopy measurements were carried out in a glovebox using a Nicolet iS5 instrument from Thermo Scientific. $FeCl_3$•$6H_2O$, 2,2,2-trifluoroethanol (TFE), 2,2,2-trifluoroethanol-*d* (TFED), thiophenol (PhSH), elemental sulfur, 2,4-pentadione (acacH), 1,4-hydroquinone (H_2Q), 2-pyrdinecarbonitrile, ethylenediamine, tetrabutylammonium hydroxide (1 M in methanol), 1,3,5-trimethoxybenzene, 2,2'-bipyridine (bpy), *N*-bromosuccinimide and 2,5-di-*tert*-butyl-hydroquinone (DTH_2Q) were purchased from Sigma Aldrich, tetrabutylammonium hexafluorophosphate ($TBAPF_6$), and $RuCl_3$•xH_2O from Fluorochem, ferrocene (Fc) and *tert*-butylimino-*tri*(pyrrolidino)phosphorene (P1 base) from ABCR, phenol (PhOH) from ACROS organics, 18-crown-6 from Apollo Scientific Ltd., 4-Chlorophenol from Fluka-Chemie AG, and $Mn(CO)_5Br$ was obtained from Sterm Chemicals. $FeCl_3.6H_2O$, acacH, 2-pyridinecarbonitrile, ethylenediamine, tetrabutylammonium hydroxide (20% aq. solution), bpy, $RuCl_3$•xH_2O, P1 base and $Mn(CO)_5Br$ were used as received. TFE, TFED and PhSH were degassed by three freeze-pump-thaw cycle before being stored over molecular sieves (4 Å) in a argon glovebox. S_8, H_2Q, DTHQ, Fc, PhOH, 1,3,5-trimethoxybenzene and 18-crown-6 were sublimed under vacuum prior to use. $TBAPF_6$ and *N*-bromosuccinamide were recrystallized from hot EtOH and hot water respectively and dried overnight under high vacuum. [bpyMn$(CO)_3$Br] (**Mn^I-cat**),[1] [$Fe_4S_4(SPh)_4$][Et_4N]$_2$ (**Fe-S** [Et_4N]$_2$),[2] PyImz (PyImz = 2- (2′-pyridyl)imidazole)[3] and [Ru^{III}(acac)$_2$(PyImz)][OTf] (**[Ru-NH$^+$]**[OTf] (acac = acetylacetonate)[4], tetrabutylammonium thiophenolate ([^{n}Bu$_4$N][SPh])[5], [K(18-crown-6)]**[Mn^{-1}-cat]**[6], tetrabutylammonium formate ((^{n}Bu$_4$N)(HCOO))[7] and the HBF_4 salt of P1 base (**P1.H$^+$**)[8] were synthesized according to the respective literature procedures.

2. Electrochemical Studies

2.1 Cyclic Voltammetry

All cyclic voltammetry (CV) experiments were performed under strictly anaerobic conditions in a conventional three electrode single-compartment cell, protected from light using aluminum foil and connected to a SP300 Bio-Logic potentiostat (Bio-Logic Science Instruments SAS). Ag/AgCl (3 M KCl) or Ag/$AgNO_3$ (10 mM in 0.1 M $TBAPF_6$ in CH_3CN) reference electrodes were used. The reference electrodes were placed in a guard compartment separated by a Vycor® frit. All potentials were referenced to an internal Fc/Fc^+ standard added in the last step of each experiment. 1 mm diameter glassy carbon electrodes (GCE, BASi) were used as working electrodes, unless otherwise specified. Electrodes were polished on wet polishing cloth using a 1 μm diamond suspension and a 0.05 μm alumina slurry before each set of experiment. The scan rate was 100 mVs^{-1} unless otherwise noted. The half-wave potentials ($E_{1/2}$) were defined as the weighing average of the corresponding cathodic peak potential (E_c) and anodic peak potential (E_a) for reversible processes. For irreversible processes, the potential at which half of the peak current ($I_c/2$) is reached, has been considered as $E_{1/2}$. In all electrochemical studies, 1 mM solutions of catalyst in CH_3CN containing 0.1 M $TBAPF_6$ as supporting electrolyte were used, unless otherwise noted.

2.1.1 CV studies: Optimization of reaction conditions

The cyclic voltammograms measured with **Fe-S** and **Mn^I-cat** separately confirmed that the redox events at -1.34 V originated from the **Fe-S**$^{0/-1}$ redox process and the remaining two events are associated with the reduction of **Mn^I-cat** to **Mn^0-dimer** and the subsequent reduction of **Mn^0-dimer** to monoanionic $[Mn(bipy)(CO)_3]^-$ (**Mn^{-1}-cat)** respectively (Fig. S1, *left*). Note that the **Fe-S** redox potential measured here varies slightly with reported data due to change of the solvent and electrolyte whereas the **Mn^I-cat** redox features match perfectly with previously reported values.[1,9] Interestingly, a shift of **Mn^I-cat** reduction processes to more cathodic potentials by ca. 50-60 mV was observed in the presence of 0.2 M TFE (Fig. S1, *right*).

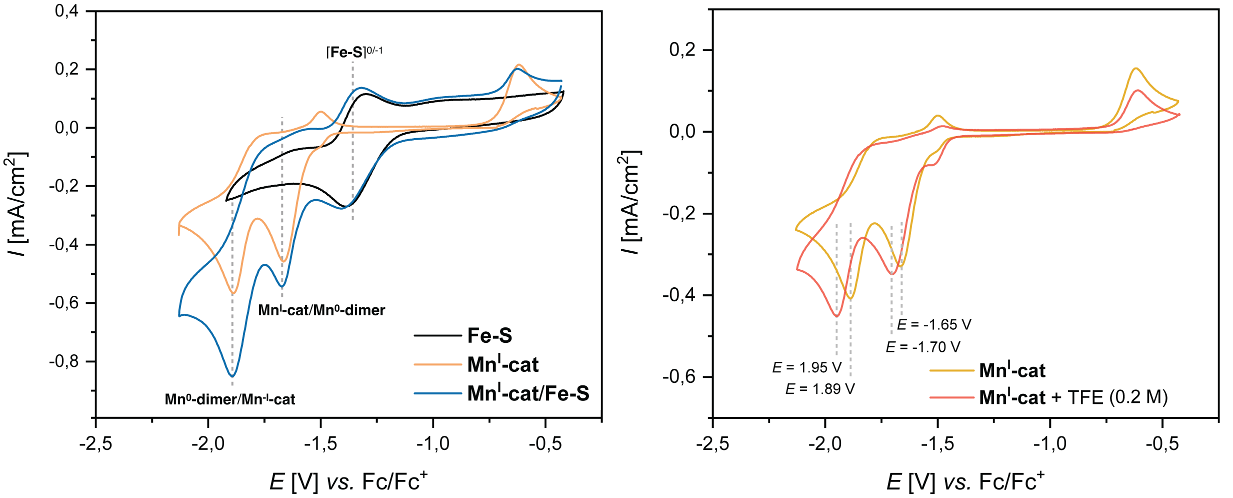

Fig. S1. (*Left*) Overlay of the CVs of 1 mM **Fe-S** (*black*), **Mn^{I}-cat** (*orange*) and a mixture of them at a 1:1 ratio (*blue*) in CH_3CN (0.1 M $TBAPF_6$) under Ar; (*Right*) Overlay of the CVs of 1 mM **Mn^{I}-cat** in CH_3CN (0.1 M $TBAPF_6$) under Ar in the absence (*orange*) and in the presence of 0.2 M TFE (*red*).

In the presence of CO_2 but in the absence of proton sources, no significant current enhancement is observed for the **Mn^{I}-cat/Fe-S** (1:1) composite solution (Fig. S2), in agreement with only trace amounts of products being detected in corresponding CPE experiments at -1.95 V ($FY_{CO} < 2\%$). This is in line with the very low activity observed for **Mn^{I}-cat** in the absence of proton sources.

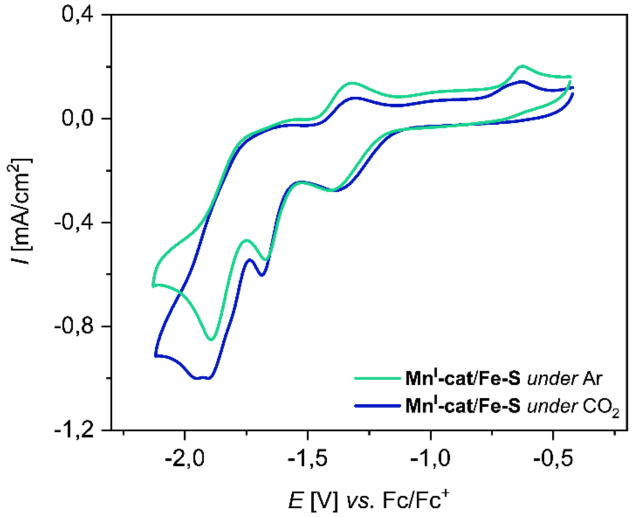

Fig. S2. Overlay of the CVs of a 1:1 mixture of **Mn^{I}-cat** and **Fe-S** under Ar (*green*) and under CO_2 (*blue*) in CH_3CN (0.1 M $TBAPF_6$).

By analogy with previous reports demonstrating that CO_2RR activity of **Mn^I-cat** being promoted in the presence of proton sources such as H_2O, TFE and PhOH,[1,10,11], we decided to investigate the activity of the **Mn^I-cat/Fe-S** (1:1) composite solution in the presence of these proton sources. In the present case, both H_2O and PhOH were found to be ineffective, as triggering the decomposition of **Fe-S** under electrochemical reduction conditions. Yet, the **Mn^I-cat/Fe-S** (1:1) composite solution displayed good stability in the presence of TFE while showing significant catalytic current enhancement (Fig. S3). We determined the optimal TFE concentration via the increase of the current at -1.85 V (Fig. S4). A steady increase of this peak was observed up to a TFE concentration of 0.3 M. Nevertheless, carrying out the same series of CVs in the presence of **Fe-S** only revealed the appearance of a large irreversible current at high concentrations of TFE (> 0.4 M) along with a loss of reversibility of the **Fe-S**$^{0/-1}$ redox process (Fig. S5) which could be attributed to the degradation of **Fe-S** upon reduction at higher TFE concentrations. To avoid such decomposition processes, an optimal TFE concentration of 0.2 M was chosen for all electrochemical studies carried out in this manuscript. In addition, we observed that the redox event at -1.85 V was also substantially increased upon increasing the **Mn^I-cat/Fe-S** ratio from 1:1 to 1:2 (Fig. 2A).

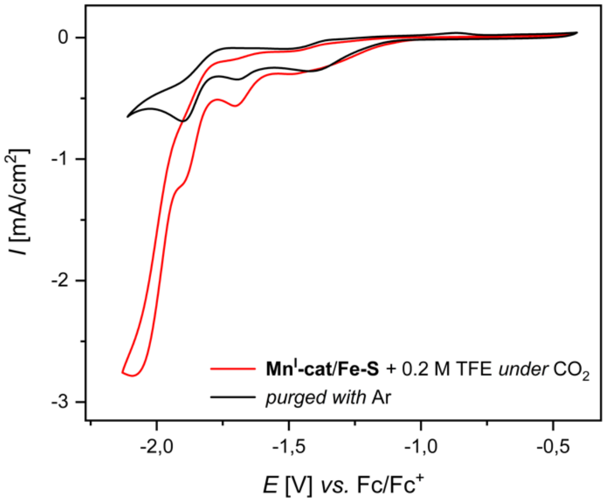

Fig. S3. Overlay of the CVs of a 1:1 mixture of **Mn^I-cat** and **Fe-S** under CO_2 in the presence of 0.2 M TFE (*red*) and after CO_2 removal by purging with Ar for 1 h (*black*).

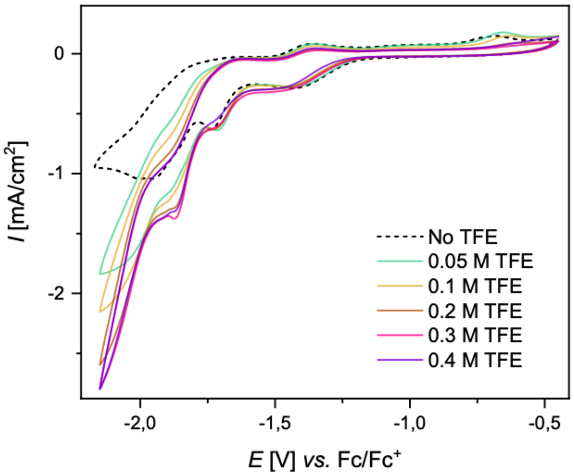

Fig. S4. Overlay of the CVs of a 1:1 mixture of **Mn^{I}-cat** and **Fe-S** under CO_2 with incremental addition of TFE (0.05 M - 0.4 M).

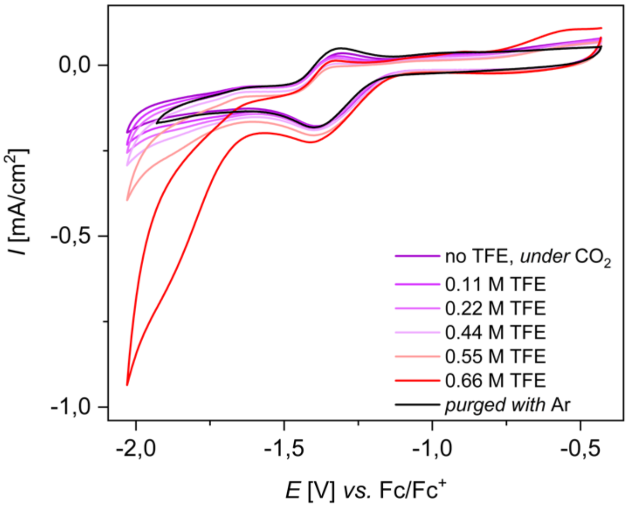

Fig. S5. Overlay of the CVs of **Fe-S** under CO_2 with incremental addition of TFE (0.11 M - 0.66 M).

Last, full removal of CO_2 via Ar bubbling led to the complete suppression of the catalytic current at -2.05 V but a substantial residual current persisted at -1.85 V (Fig. S6), indicating an enhanced H_2 evolution activity of **Mn^{I}-cat** in the presence of **Fe-S**.

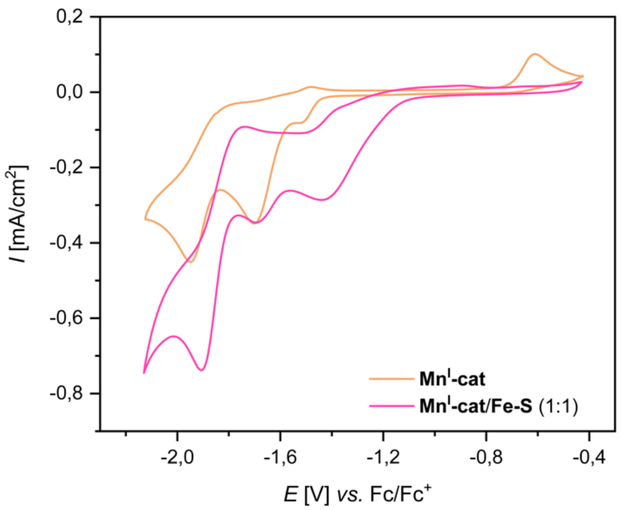

Fig. S6. Overlay of the CVs of **Mn^{I}-cat** (*orange*) and of a 1:1 mixture of **Mn^{I}-cat** and **Fe-S** (*pink*) under Ar in the presence of 0.2 M TFE.

2.2 Controlled Potential Electrolysis (CPE)

Bulk electrolysis experiments were performed using a custom-built gastight H-type cell loaded in a glovebox with its two compartments separated by two Ceramic-PVDF Composite membranes (16 µm thickness, Xuran). A 0.5 mm diameter platinum wire (10 cm length) was used as the counter electrode and placed in the anodic compartment. A glassy carbon plate (GCP) electrode (A = 1.4 cm^2) was used as the working electrode in the cathodic compartment for the optimization of the catalytic efficiency unless otherwise mentioned. The cell was purged with Ar or CO_2 for a minimum of 30 min. prior to controlled potential electrolysis. Constant magnetic stirring of 600 rpm with a rice grain-type stir bar was applied during electrolysis. A 1 mM concentration of **Mn^I-cat** was used for all CPEs unless otherwise mentioned, and the **Fe-S** concentrations were adjusted accordingly to obtain the desired **Mn^I-cat**/**Fe-S** ratios.

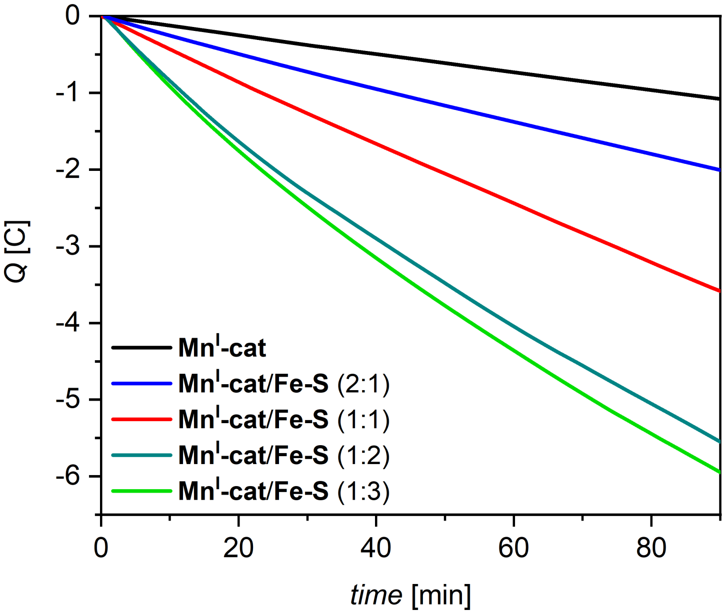

Fig. S7. Overlay of the CPE data as charge Q *vs*. time plots obtained with increasing ratios of **Fe-S** to **Mn^I-cat** under CO_2 and in the presence of 0.2 M TFE.

2.3 Product detection

The headspace of the electrolysis H-cell was analyzed by gas chromatography (Multi-Gas Analyzer #5; SRI Instruments), equipped with Haysep D and MolSieve 5 Å columns and thermal conductivity detector (TCD) and flame ionization detector (FID) coupled with a methanizer using argon or N_2 as carrier gas. The typical volume of injected gas was 50 µL from the headspace, sampled using a gastight syringe. Formic acid (HCOOH) was quantified using ion exchange chromatography (883 Basic IC; Metrohm) and ^{1}H-NMR.

IC measurements were carried out after 50 times dilution of the electrolyzed solution in acetonitrile with MiliQ H_2O.

NMR samples were prepared using 300 µL of the electrolyzed solution, to which 100 µL of acetonitrile-d_3 and 100 µL of 20 mM TMB (1,3,5-trimethoxybenzene) in acetonitrile as internal standard were added. Solvent suppression sequence (pre-saturation on the CH_3CN signal $\delta = 1.97$ ppm) was used. A calibration curve for the detection of formate was determined from the ratio between the area of the formate C-H peak and the aromatic proton signal of 1,3,5-trimethoxybenzene using increasing concentrations of $(^{n}Bu_4N)(HCOO)$. The amount of formate/formic acid generated in the catalytic test was then determined using this calibration curve.

It should be noted that both IC and NMR techniques do not allow determining if formate or formic acid are formed. We used here FTIR to discriminate these two reaction products, as both species show distinct IR features. We determined the IR stretches for both species under the same conditions as used in the electrocatalytic tests (CH_3CN/0.1 M $(^{n}Bu_4N)PF_6$ - 0.2 M TFE). As highlighted in Fig S8, a 4 mM solution of $(^{n}Bu_4N)(HCOO)$ displays an IR stretch at 1608 cm^{-1} ($\nu_S(C=O)$) whereas the $\nu_S(C=O)$ stretch of formic acid appears at 1710 cm^{-1} under similar condition. The later value is in good agreement with the $\nu_S(C=O)$ stretch value (1700 cm^{-1}) observed during IRSEC experiments, highlighting the formation of formic acid in catalytic conditions (*vide infra*).

The protonation of formate by TFE in the catalytic conditions could be independently demonstrated upon purging a solution of tetrabutylammonium formate in the electrolyte solution used here (CH_3CN/0.1 M $(^{n}Bu_4N)PF_6$ - 0.2 M TFE) with CO_2 for 30 min. The intensity of the $\nu_S(C=O)$ stretch of formate at 1608 cm^{-1} decreased while a new broad stretch appeared at 1691 cm^{-1}. The broadening of the stretches may result from hydrogen bonding of HCOOH with $HCOO^-$ and $CF_3CH_2O\text{-}CO_2^-$.

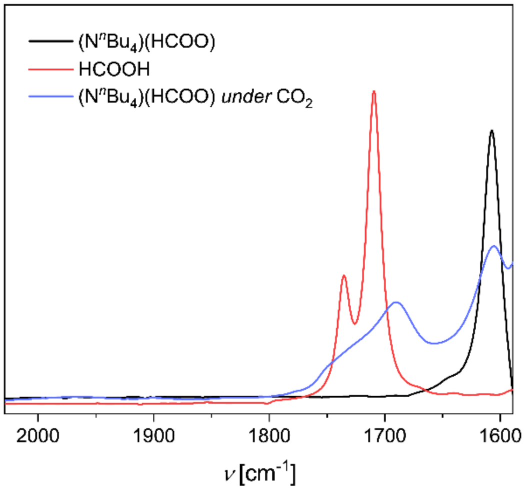

Fig S8: Overlay of the IR data recorded for (^{n}Bu$_4$N)(HCOO) *(black trace*) and formic acid (*red trace*) under the catalytic conditions used in this work (CH$_3$CN/0.1 M TBAPF$_6$ - 0.08 M TFE under Ar). The blue spectrum was obtained upon 30 min purging of CO$_2$ into the solution used for measurement of the black spectrum.

2.4 Faradaic yield calculation

The faradaic yield (FY) of a catalytic reaction was determined by the eq. below assuming a two e^- reduction process is involved here:

$$\text{FY (in \%)} = 100 \times \frac{2 \times n_{\text{product}} \times F}{Q_{\text{tot}}} \qquad \text{(i)}$$

$$\text{FY}_{\text{HCOOH}}\ \text{(in \%)} = 100 \times \frac{2 \times n_{\text{HCOOH}} \times F}{Q_{\text{tot}}} \qquad \text{(ii)}$$

where n_{product} is the amount of product formed in moles (*i.e.* n_{HCOOH} in case of HCOOH), F is the faradaic constant and Q_{tot} the total amount of charge passed during CPE.

The charge dedicated to the generation of the actual catalyst but not consumed in the catalytic cycle was deducted from the total charge passed in the equation above. This is illustrated for the example below: During the CPE of the **Mn$^{\mathbf{I}}$-cat/Fe-S** (1:1) mixture at -1.85 V *vs.* Fc/Fc$^+$, the total charge consumed was 3.58 C after 90 minutes. 13.6 ± 1.1 µmol of HCOOH and 1.43 ± 0.18 µmol of CO were quantified as the products of this CPE experiment. According to our proposed reaction mechanism, one equivalent of electrons is required to generate the active catalyst and it is hence not contributing to the catalytic turnover. In other words, in the first turnover, three equivalents of charge are required to generate one equiv. of products. Hence, this amount of charge should be deducted from the total charge passed in the equation mentioned above. The present CPE was performed using a 1 mM solution of **Fe-S** (**Mn^{I}-cat/Fe-S** (1:1) ratio) in 6 mL of volume, which implies the subtraction of 0.58 C of charge from the total charge passed. The FY was hence determined accordingly:

$$\mathrm{FY_{HCOOH}} = 100 \times \frac{2 \times (13.6 \pm 1.1) \times 96485}{(3.58 - 0.58) \times 10^{6}}$$

$$\mathrm{FY_{HCOOH}} = 87 \pm 7\%$$

Similarly,

$$\mathrm{FY_{CO}} = 9.5 \pm 1\%$$

Note that varying the **Mn^{I}-cat/Fe-S** ratio impacts the charge to be subtracted as not contributing to the catalytic cycle: in the case of the **Mn^{I}-cat/Fe-S** (2:1) ratio, only ca. 0.3 C of charge is subtracted as half an equiv. of charge is required to trigger the generation of the active CPET mediator. This method of calculation holds reasonably well up to a **Mn^{I}-cat/Fe-S** (1:2) ratio while a slightly lower FY for **Mn^{I}-cat/Fe-S** (1:3) is observed, in agreement with the reduction of a larger amount of **Fe-S** not active in the CPET transfer cycle.

Errors associated to CPE FY and product yields were determined from duplicate independent CPE experiments as well as evaluating systematic errors on each measurement by triple consecutive measurements of the same sample by IC (HCOOH) or GC (CO, H_2). The average value from these measurements enabled the determination of FY and product yields reported in this work, as well as associated standard deviation values, reported in the corresponding plots as error bars.

Table S1. Product analysis after 90 minutes CPE in presence of a series of catalyst/CPET mediator mixtures. The CPEs were performed in the presence of 0.2 M TFE.

	Catalyst	E_{CPE} [V]	Q_{CPE} [C]	Product yield [μmol]			FY (%)				$\mathrm{TON_{CO}}^{a}$	$\mathrm{TON_{HCOOH}}^{a}$	HCOOH:CO ratio
				CO	HCOOH	H_2	CO	HCOOH	H_2	Total			
1	**$\mathrm{Mn^{I}}$-cat**	-1.85	1.09	5.12	-	-	91	-	-	91	0.85	0	0:1
2	**Fe-S** (2mM)	-1.85	1.25	0.01	1.92	1.08	< 1	29.6	16.8	47	0^{b}	0.2^{b}	1:0
3	**$\mathrm{Mn^{I}}$-cat/Fe-S** (2:1)	-1.85	1.99	2.09	4.42	-	28.7	60.8	-	90	0.33	0.75	2.1:1
4	**$\mathrm{Mn^{I}}$-cat/Fe-S** (1:1)	-1.85	3.59	1.43	13.38	-	9.3	86.8	-	96	0.24	2.23	9.3:1
5	**$\mathrm{Mn^{I}}$-cat/Fe-S** (1:2)	-1.85	5.57	1.67	23.16	-	6.5	91.5	-	98	0.28	3.85	13.9:1
6	**$\mathrm{Mn^{I}}$-cat/Fe-S** (1:3)	-1.85	5.97	1.59	23.85	-	5.6	85.3	-	91	0.27	3.98	15:1
7	**$\mathrm{Mn^{I}}$-cat/Fe-S** (1:2)	-1.7	2.01	0.71	9.46	-	6.7	90.8	-	97	0.11	1.57	13.4:1
8	**$\mathrm{Mn^{I}}$-cat/Fe-S** (1:2)	-1.65	1.94	0.38	7.61	-	3.4	78	-	81	0.06	1.27	20:1
9	**$\mathrm{Mn^{I}}$-cat/Fe-S** (1:2)	-2.05	8.19	12.53	22.17	2.46	31.8	56.4	6.2	94	2.08	3.7	1.8:1
10	**$\mathrm{Mn^{I}}$-cat**/$\mathrm{SPh^{-}}$ (1:1)	-1.85	1.89	6.62	2.0	-	67.6	20.5	-	88	1.1	0.33	1:3.3
11	**$\mathrm{Mn^{I}}$-cat/Fe-S** (1:2) Under Ar	-1.85	1.78	0.19	-	3.01	3	-	49.3	52.3	0.03	-	N.A.

[a] TON calculated with respect to the amount of **$\mathrm{Mn^{I}}$-cat**, according to section 2.7 below, unless otherwise specified. [b] TON calculated with respect to **Fe-S**.

2.5 Determination of standard reduction potential of CO_2/HCOOH couple and overpotential

Based on simple free energy calculation, the standard potential of the CO_2/HCOOH couple in CH_3CN can be determined by the following equation:[12]

$$E^{0}_{\frac{\mathrm{CO2}}{\mathrm{HCOOH}}}(\mathrm{CH_3CN, AH}) = -0.15\ \mathrm{V} - 0.059 \times \mathrm{p}K_{\mathrm{a}}(\mathrm{AH})\ \mathrm{V}\ vs. Fc/Fc^{+} \qquad \text{(iii)}$$

Here, formic acid, generated via a $2e^{-}/2H^{+}$ process, is observed as the major product, confirming the applicability of the above equation. TFE is used as the proton source (HA). Considering the theoretically determined pK_a value for TFE in CO_2 saturated CH_3CN of 25.1,[13,14] we finally obtain:

$$E^{0}_{\mathrm{CO2/HCOOH}}(\mathrm{CH_3CN, AH}) = -1.63\ \mathrm{V}\ vs.\ \mathrm{Fc/Fc^{+}}. \qquad \text{(iv)}$$

The overpotential for formic acid (η) is hence expressed as $\eta = \left|E_{\mathrm{appl}} - E^{0}_{\mathrm{CO_2/HCOOH}}\right|$.

The E_{CPE} = -1.85 V and E_{CPE} = -1.65 V *vs.* Fc/Fc^{+} are applied here, in agreement with η values of 0.22 V and 0.02 V respectively. Nevertheless, as the pK_a of TFE has only been estimated by theoretical calculations and not experimentally determined, overpotential values provided by this calculation should be considered with care, as a certain error could originate from the deviation of the actual pK_a value of TFE *vs.* the theoretical value used for calculation. In particular, the formation of HCOOH highlights that the predicted pK_a values for formic acid (20.9)[15] and TFE (25.1)[14] likely differ from the actual pK_a values of these species under conditions used herein. Nevertheless, the accurate determination of the pK_a values of these species in the electrolytic solution is not straightforward, especially in the presence of CO_2, as strong homoconjugation of the acids in such a non-aqueous solvent media significantly impact their pK_a values. This is well exemplified in the case of TFE, for which a lowering of ca. 10 pK_a units has been proposed theoretically in the presence of CO_2 (from 35.8 to 25.1).[14]

In order to estimate this error in the present work, we determined the pK_a of HCOOH in the catalytic conditions as the direct determination of the pK_a of TFE in the presence of CO_2 was too complex owing to the interaction of most bases used for titration with CO_2.

We determined the pK_a of formic acid by NMR titration of a 4 mM solution of [$Ru^{II}(acac)_2(PyImz)$] (**Ru-NH**) (pK_a = 22.1) [4] in CH_3CN (1 mL) containing 0.1 M $TBAPF_6$ using ($^n Bu_4N$)(HCOO) (Fig. S9). The extent of deprotonation of **Ru-NH** was evaluated according to the analysis of the chemical shift variation of selected aromatic signals of the PyImz ligand, as the NMR nuclei near the basic site sense a different electronic environment upon protonation. Since protonation processes are fast on the NMR timescale, the observed chemical shift can be expressed as a weighted average of chemical shifts of the protonated (**Ru-NH**) and deprotonated (**Ru-N**$^-$) form, according to the following general expression:

$$\delta_{\text{obs}} = \delta_{\mathbf{Ru-NH}} \times \chi_{\mathbf{Ru-NH}} + \delta_{\mathbf{Ru-N^-}} \times \chi_{\mathbf{Ru-N^-}} \qquad \text{(v)}$$

where δ_{obs} is the observed chemical shift, and $\delta_{\mathbf{Ru-NH}}$, $\delta_{\mathbf{Ru-N^-}}$ and $\chi_{\mathbf{Ru-NH}}$, $\chi_{\mathbf{Ru-N^-}}$ are the chemical shifts and mole fractions of the corresponding species, respectively.

Expressing $\chi_{\mathbf{Ru-NH}}$ and $\chi_{\mathbf{Ru-N^-}}$ as a function of the extent of reaction ξ for the following equilibrium:

$$\mathbf{Ru\text{-}NH} + HCOO^- \rightleftharpoons \mathbf{Ru\text{-}N^-} + HCOOH \qquad \text{(vi)}$$

, δ_{obs} can be expressed as:

$$\delta_{\text{obs}} = \delta_{\mathbf{Ru-NH}} \times \frac{(n-\xi)}{n} + \delta_{\mathbf{Ru-N^-}} \times \frac{\xi}{n} \qquad \text{(vii)}$$

, where n is the initial amount of **Ru-NH** used in the experiment. Accordingly:

$$\xi = \frac{n \times (\delta_{\text{obs}} - \delta_{\mathbf{Ru-NH}})}{(\delta_{\mathbf{Ru-N^-}} - \delta_{\mathbf{Ru-NH}})} \qquad \text{(viii)}$$

Equation (viii) enables to determine ξ as a function of n_{HCOO^-} which is the amount of ($^n Bu_4N$)(HCOO) added to the NMR sample (Fig. S9 and Table S2).

In addition, considering equation (vi) at equilibrium, ξ can be expressed as the following expression:

$$\xi = \frac{-K(n+n_{\mathrm{HCOO^-}})+\sqrt{(K(n+n_{\mathrm{HCOO^-}}))^2+4(1-K)(K\times n\times n_{\mathrm{HCOO^-}})}}{2(1-K)} \qquad \text{(ix)}$$

, where K is the equilibrium constant of reaction (vi).

Least square minimization of the mean ξ values determined by NMR using equation (ix) with the Excel solver add-on allowed determining a K value of 2.915, corresponding to a pK_a value of ca. 21.6 for HCOOH, given the determined pK_a value for **Ru-NH** of 22.1 .[4]

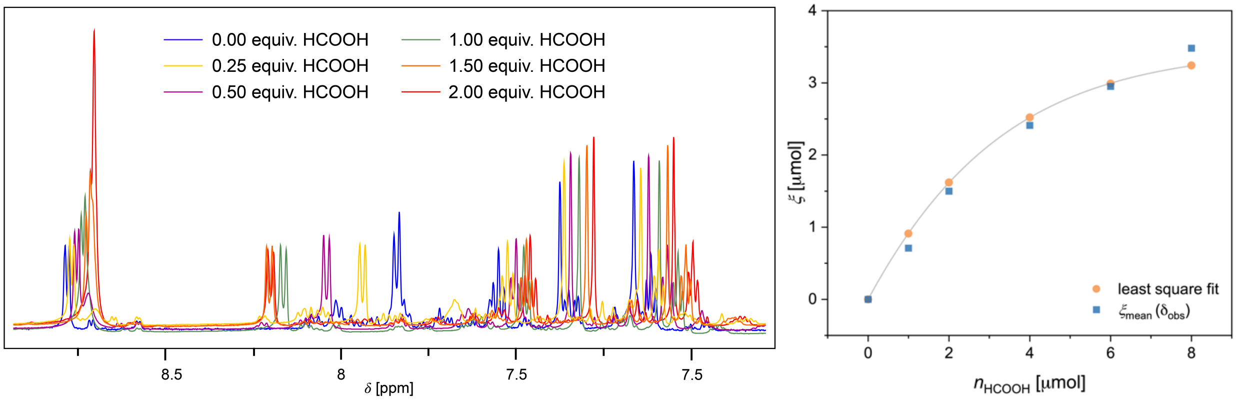

Fig. S9. (*left*) Chemical shift variation of the PyImz ligand signals of **Ru-NH** upon addition of (^{n}Bu$_4$N)(HCOO) and (*right*) plot of the mean ξ values determined by NMR according to equation (viii) and corresponding least square minimization using the equation (ix) with the Excel solver add-on (K = 2.915).

Table S2. Chemical shift variation of the PyImz ligand signals of a 4 mM solution of **Ru-NH** upon addition of (^{n}Bu$_4$N)(HCOO) and corresponding ξ values and least square minimization using the equation (ix) with the Excel solver add-on (K = 2.915).

(^{n}Bu$_4$N)(HCOO) [μmol]	**7.11 ppm (t)^a**		**7.16 ppm (s)^a**		**7.37 ppm (s)^a**		**7.55 ppm (t)^a**		**7.85 ppm (d)^a**		**8.78 ppm (d)^a**		**$\xi_{\mathrm{mean}}{}^c$**	**Least square fit**
	δ_{obs}	ξ^b	δ_{obs}	ξ^b	δ_{obs}	ξ^b	δ_{obs}	ξ^b	δ_{obs}	ξ^b	δ_{obs}	ξ^b		
0	7.115	0.00	7.165	0.00	7.377	0.00	7.550	0.00	7.849	0.00	8.786	0.00	0.00	0.00
1	7.093	0.61	7.145	0.56	7.365	0.41	7.524	1.02	7.945	1.01	8.773	0.62	0.71	0.91
2	7.069	1.28	7.122	1.19	7.346	1.06	7.499	2.01	8.048	2.09	8.758	1.34	1.50	1.62
4	7.039	2.11	7.092	2.02	7.322	1.88	7.477	2.85	8.171	3.38	8.7340	2.23	2.41	2.52
6	7.016	2.73	7.068	2.69	7.3	2.63	7.470	3.19	8.190	3.58	8.726	2.89	2.95	2.99
8	6.996	3.28	7.049	3.21	7.277	3.42	7.459	3.63	8.207	3.76	8.711	3.59	3.48	3.24

^{a} peaks are referred to as their chemical shift values in the absence of (^{n}Bu$_4$N)(HCOO). ^{b} Determined using equation (viii). ^{c} mean ξ values for the NMR peaks of the PyImz ligand of **Ru-NH** reported in this table.

Under catalytic conditions, the TFE concentration (0.2 M) is ca. two orders of magnitude higher than the formate concentration (in the mM range). To enable the formation of HCOOH in significant amounts such as observed in catalytic conditions or in the FTIR studies presented in section 2.3 above, a maximum difference of ca. 2 pK_a units between HCOOH and the proton source in solution should be present, allowing to estimate a higher limit for the pK_a of the electrolytic solution of ca. 23.6. In addition, the sluggish regeneration of the **Ru-NH** mediator in the presence of TFE suggests a lowest boundary for the pK_a of the proton source in solution that can be expected to be at least one pK_a unit above the pK_a of the mediator. Combining these two observations, we estimated that the actual pK_a of TFE in the catalytic condition used here may differ from the proposed value of 25.1[14] and instead lays in the range of 23-23.6. Using this value instead of the previously reported one translates in an additional overpotential of 120 mV. To account for this uncertainties in the actual value of pK_a(AH) in equation (iii), all overpotential values determined in this work are given as a range of overpotentials, the lowest overpotential being calculated considering the reported pK_a value of TFE of 25.1 as reported above and the highest overpotential accounting for this additional 120 mV contribution. Note that as several overpotential data taken from literature and presented in Table S3 and Fig 2F have been determined using the theoretical value for TFE mentioned above, and may suffer from the same uncertainties in the determination of overpotential values.

2.6 Turnover frequency determination from controlled potential electrolysis experiments

A stable current during CPE prompted us to use the following formula to calculating the TOF as global TOF of the process:[13]

$$\mathrm{TOF}_{\mathrm{Average}} = k_{\mathrm{cat}} = \frac{i^2}{F^2 D [\mathrm{cat}]^2 A^2} \qquad \text{(x)}$$

, where i is the average of the stable current density during a CPE experiment (1.4 ± 0.1 mA as obtained in prolonged electrolysis at -1.85 V for 2.5 h using a 1:2 **Mn$^{\mathrm{I}}$-cat/Fe-S** ratio), F is the Faraday constant (96485 $\mathrm{A \cdot s \cdot mol^{-1}}$), A is the surface of the GC-plate electrode used (2 $\mathrm{cm^2}$), [cat] is the concentration of catalyst (1 mM = 1 x 10^{-6} $\mathrm{mol \cdot cm^{-3}}$) and D is the diffusion coefficient of **Mn$^{\mathrm{I}}$-cat**. D was determined from the slope of $i_{\mathrm{p}} = f(v^{1/2})$ as 5.2 x 10^{-6} $\mathrm{cm^2 \cdot s^{-1}}$. Accordingly, the TOF was calculated to be **20.3 ± 2 $\mathrm{s^{-1}}$** at -1.85 V.

Using the same method, the TOF obtained during CPE using the same 1:2 **Mn$^{\mathrm{I}}$-cat/Fe-S** system and was determined to be **0.46 $\mathrm{s^{-1}}$** at -1.7 V and **0.4 $\mathrm{s^{-1}}$** at -1.65 V.

2.7 Turnover number determination

The turnover number (TON) for HCOOH using the composite catalytic systems used here can be determined by using the equation below :

$$\mathrm{TON}_{HCOOH} = \frac{n_{\mathrm{HCOOH}}}{n_{\mathrm{cat}}} \qquad \text{(xi)}$$

where n_{HCOOH} is the amount of HCOOH formed and n_{cat} the amount of **Mn$^{\mathrm{I}}$-cat** used for CPE, both in moles. As an example, over 2.5 h CPE using a 2 $\mathrm{cm^2}$ GCP working electrode and the **Mn$^{\mathrm{I}}$-cat/Fe-S** (1:2) composite solution at -1.85 V, a total amount of 3.95 µmol. of CO and 56.4 µmol of formic acid was quantified, at the expense of 13.22 C of charge. A 6 mL solution of of 1 mmol **Mn$^{\mathrm{I}}$-cat** and 2 mM **Fe-S** mixture solution was used, accounting for an amount of 6 µmol of catalyst. From these data, a **TON$_{\mathrm{HCOOH}}$** of **9.4 ± 0.6** for formic acid and **0.65 ± 0.1** for CO was determined (Fig. S10).

TON values for CO can be calculated according to the same equation. TON values after 90 min are provided in Table S1.

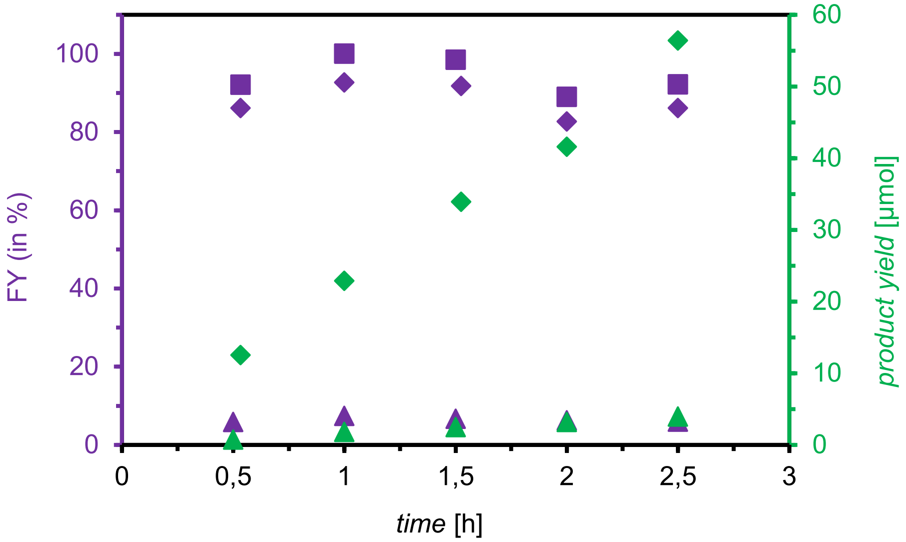

Fig. S10. Evolution of the amount of products generated over 2.5 h CPE at -1.85 V using 2 cm^2 GCP electrode (*green symbols*). Respective and total FYs are given in *purple symbols*. Triangle shapes indicate data for CO while the diamond shape is used for formic acid. The total FY is given by the purple squares.

2.8 Catalytic efficiency comparison

We benchmarked the catalytic performances of the catalytic systems reported in this work against other molecular catalysts using a catalytic Tafel plot, correlating TOF and overpotential η.[16,17] As the complexes reported in this manuscript show selectivity for HCOOH below unity, we use here an adapted log(TOF) *vs.* η approach taking into account of the partial current density for formic acid generation as introduced in our previous work [18]:

$$\mathrm{TOF} = Ai^2 \qquad \text{(xii)}$$

$$i_{\mathrm{HCOOH}} = i \times FY_{\mathrm{HCOOH}} \qquad \text{(xiii)}$$

$$\mathrm{TOF}_{\mathrm{HCOOH}} = A(i_{\mathrm{HCOOH}})^2 = A(i \times FY_{\mathrm{HCOOH}})^2 = A[\mathrm{TOF} \times (FY_{\mathrm{HCOOH}})^2] \qquad \text{(xiv)}$$

This approach enables to determine the values required to generate the log(TOF) *vs.* η plot shown in Fig. 2F using the values reported for known electrocatalysts promoting CO_2RR to HCOOH provided in Table S3.

Table S3. List of complexes with corresponding overpotentials and TOF values used to establish the log[TOF/s^{-1} (FY$_{\mathrm{HCOOH}}$)^2] *vs.* overpotential (η) plot shown in Fig. 2F.

Catalyst	**max. FY** [%]	**TOF** [s^{-1}]	**Overpotential *η*** [mV]	**ref.**
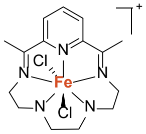 **[FeN$_5$Cl$_2$]$^+$**	80	0.3	310	19
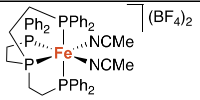 **[FeP$_4$N$_2$]$^{2+}$**	97.5	2.8	500	20
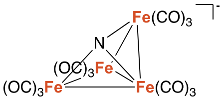 **[Fe$_4$N(CO)$_{12}$]$^-$**	96	11	180	21
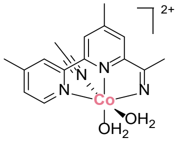 **[Co(imino-bpy)]$^{2+}$**	80	11	480	22
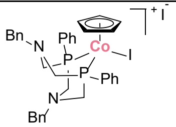 **[CoCp(P$_2$N$_2$)]$^{2+}$**	92	10^3	750	17
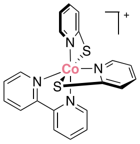 **[(bipy)Co(PyS)$_2$]$^+$**	64	27.5	190	18
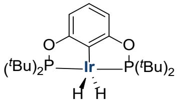 **[Ir(POCOP)]$^{2+}$**	85	20	680	23
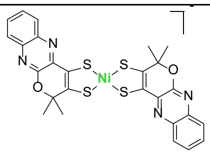 **[Ni(qpdt)$_2$]$^-$**	60	89	540	13
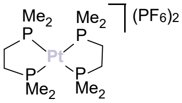 **[Pt(dmpe)$_2$]$^{2+}$**	90	0.5	90	24

2.9. Catalyst stability studies

2.9.1 Rinse test

A 90 min CPE at -1.85 V with a solution of **Mn^{I}-cat/Fe-S** (1:2) in CO_2 saturated CH_3CN (0.1 M $TBAPF_6$). was carried out using a GCP electrode as described in section 3.2. After that CPE step, the electrolyzed solution was syringed out from both compartments under a flow of CO_2 and another 6 mL of fresh catalyst-free electrolyte solution (0.1 M $TBAPF_6$ in CH_3CN) was replaced in each compartment. After bubbling CO_2 through this solution for 30 min, a second 90 min electrolysis was performed at the same potential. Current *vs.* time and corresponding charge *vs.* time plots for both experiments are given below in Fig. S11. A significant drop in current is observed in the absence of the catalyst, showing similar CO_2RR background current and activity as observed with independently run blank experiment using fresh GCP electrodes, confirming that the CO_2RR catalytic activity observed originates from soluble catalyst species (Table S4).

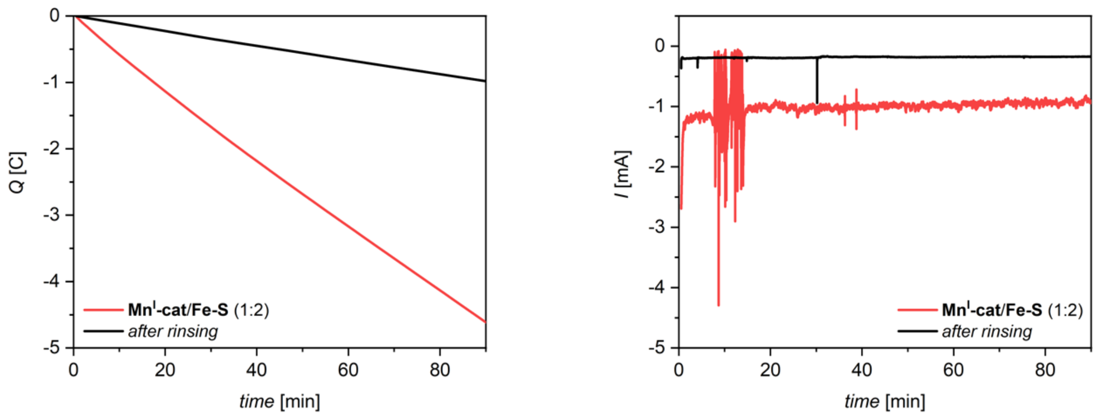

Fig. S11. Overlay of the CPE data in charge *vs.* time (*left*) and current *vs.* time (*right*) for the 1:2 **Mn^{I}-cat/Fe-S** mixture (*red*) under catalytic condition (CO_2/0.2 M TFE in CH_3CN/0.1 M $TBAPF_6$) and after rinsing the CPE cell with fresh electrolyte (*black*).

Table S4. Product analysis of rinse-test experiments

Entry	Catalyst	E_{CPE} [V] *vs.* Fc/Fc$^+$	Q_{CPE} [C]	Products formed [µmol]			FY (%)			
				CO	HCOOH	H_2	CO	HCOOH	H_2	Total
1	**Mn^{I}-cat/Fe-S** (1:2)	-1.85	4.61	1.85	18.237	-	7.6	87.7	-	95.3
2	After rinsing	-1.85	0.803	0.016	1.017	1.872	< 1	24.5	45	70
3	GCP electrode only	-1.85	0.394	0.023	0.9394	-	1.1	46	-	47

2.9.2 Influence of thiophenolate ligand

To rule out that the selectivity shift from CO to HCOOH originates from ligand exchange between **Fe-S** and **Mn^{I}-cat**, a set of CV and CPE experiments using **Mn^{I}-cat** in the presence of 1 equiv. of tetrabutylammonium thiophenolate ($[^{n}\text{Bu}_4\text{N}][\text{SPh}]$) were carried out. The CV data are given below (Fig. S12), showing a current enhancement at potentials below -1.8 V. Corresponding product analysis after CPE at -1.85 V (Table S1) revealed that the major product was still CO as previously reported with exogenous anionic ligands *e.g.* CN^{-}.[25] This excludes the possibility of any artefact arising due to the hydrolysis of the thiophenolate moiety from the **Fe-S** core.

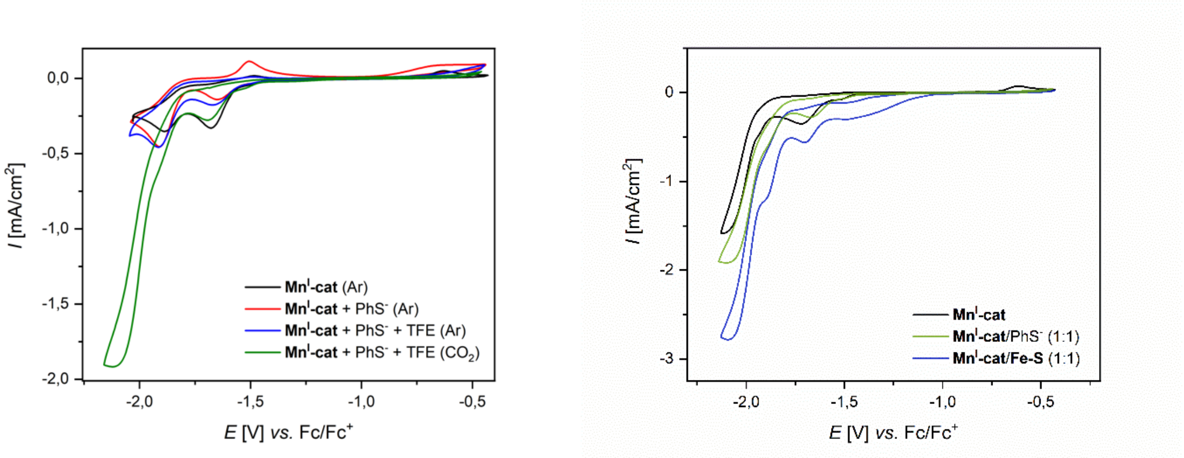

Fig. S12. Overlay of the CVs obtained upon addition of 1 equiv. $[^{n}\text{Bu}_4\text{N}][\text{SPh}]$ to **Mn^{I}-cat** under Ar and CO$_2$ (*left*) and in the presence of proton source (0.2 M TFE). Comparison of the CVs of **Mn^{I}-cat**, **Mn^{I}-cat/SPh^{-}** (1:1) and **Mn^{I}-cat/Fe-S** (1:1) under optimized catalytic conditions (CO$_2$ saturated CH_3CN , 0.1 M TBAPF$_6$, 0.2 M TFE) (*right*).

3. Infrared spectro-electrochemistry experiments

Infrared spectro-electrochemistry (IR-SEC) experiments were performed using 2 mM solutions of **Mn^I-cat** in CH_3CN containing 0.1 M $TBAPF_6$ as supporting electrolyte. Accordingly, 4 mM concentrations of **Fe-S** were used for **Mn^I-cat/ Fe-S** (1:2) experiments. The experiments were carried out in a LabOmak UF SEC cell with a Pt-mesh working- and counter electrode. A Ag-wire was used as pseudo reference electrode. The potential of the Ag-wire pseudo reference electrode was determined for each experiment by introduction of a 5 mM Fc solution into the IRSEC cell; and potentials are reported *vs.* the measured Fc/Fc^+ redox potential. Throughout the experiment series reported here, only minor potential variations were observed for the redox potential of the Fc/Fc^+ couple, varying within the range 740 mV to 690 mV.

For CO_2 reduction experiments, the CH_3CN (0.1 M $TBAPF_6$) solutions were pre-saturated with CO_2 by a 30 min purging cycle prior to be introduced in the IR-SEC cell. The data were recorded after a short CPE (30 s to 4 min). For the studies in the presence of proton source, the required amount of TFE was added to the solution just before injection into the IR-SEC cell.

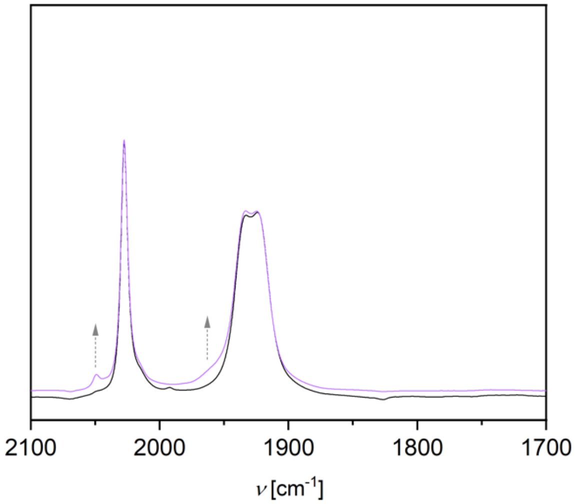

Fig. S13: Overlay of the IRSEC data acquired for **Mn^I-cat/Fe-S** (1:2) in CO_2 saturated CH_3CN (0.1 M $TBAPF_6$, 0.08 M TFE) at -1.3 V (*purple line*) and at open circuit potential (*black*).

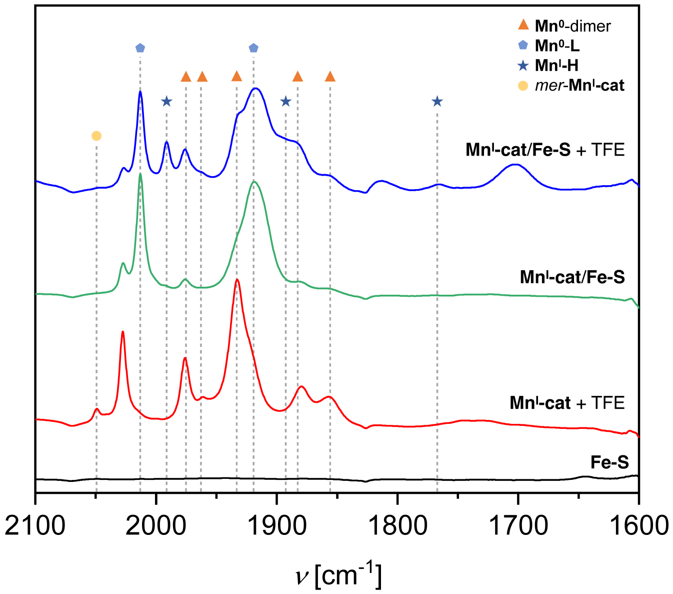

Fig. S14. Overlay of the IRSEC data recorded after 4 min CPE at -1.65 V with **Fe-S** (4 mM), **Mn^{I}-cat** (2 mM) and **Mn^{I}-cat/Fe-S** (1:2) mixture in the presence and the absence of TFE (0.08 M) under CO_2.

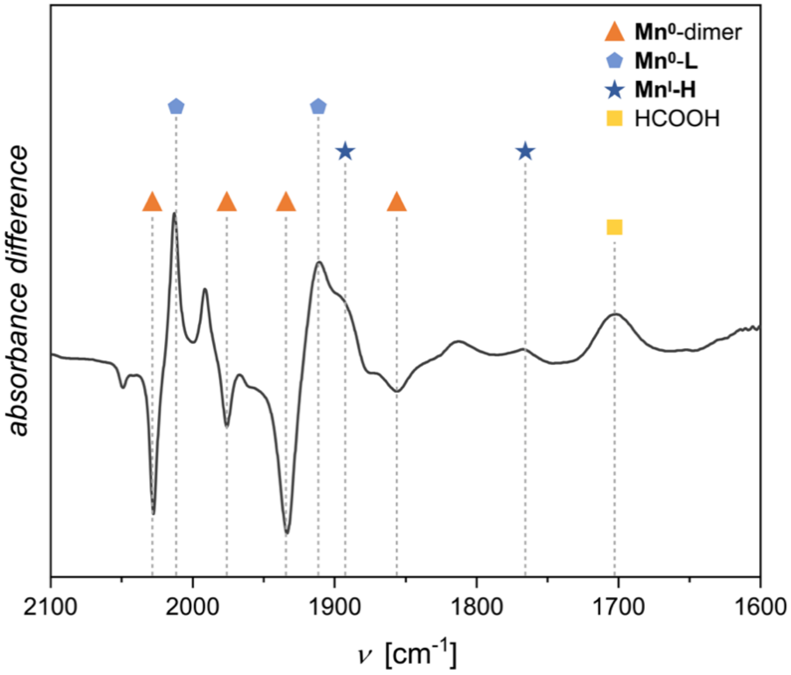

Fig. S15. Difference of the FTIR spectra obtained for **Mn^{I}-cat** after 4 min CPE at -1.65 V in the presence and the absence of **Fe-S** under CO_2 and in the presence of TFE (0.08 M).

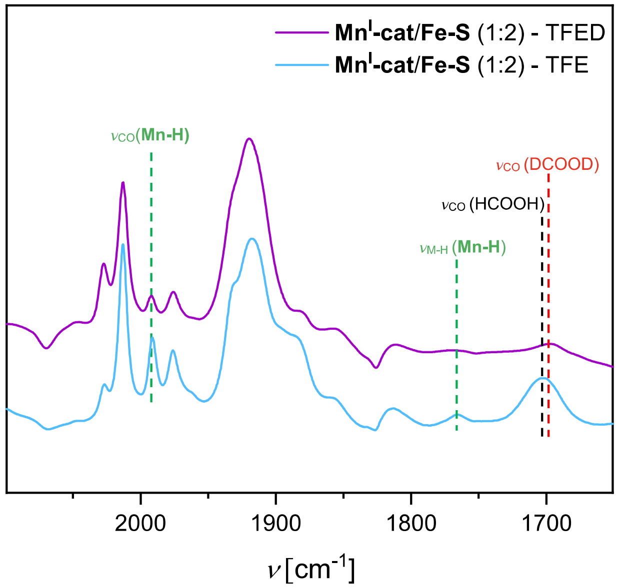

Fig. S16. Overlay of the IRSEC data recorded after 4 min CPE at -1.65 V using a **Mn^{I}-cat/Fe-S** (1:2) mixture in the presence of TFE (*blue*) or TFED (*purple*) (0.08 M) under CO$_2$.

Table S5. Reported and experimental ν_{CO} stretching frequencies for relevant Mn complexes.

Reported species	$\nu_{CO}^{reported}$[cm^{-1}]		**Species identified (*this work*)**	$\nu_{CO}^{observed}$[cm^{-1}]
fac-^{tBu}bpyMn^{I}(CO)$_3$Br	2028, 1933, 1923		*fac*-**Mn^{I}-cat**	2028, 1932, 1923
fac-Mn^{I}-cat	2027, 1933, 1924			
fac-^{OH}bpyMn(CO)$_3$(CH$_3$CN)]$^{+}$	2045, 1955		*mer*-**bpyMn^{I}(CO)$_3$Br**	2049, 1952
mer-^{PMO}bpyMn^{I}(CO)$_3$Br	2049, 1946			
[Mn^{0}-dimer]^{a}	1975, 1963, 1936, 1886, 1866	*vs.*	**Mn^{0}-dimer**	1975, 1963, 1934, 1878, 1853
[Mn(pdbpy)(CO)$_3$(CH$_3$CN)]^{b}	2014, 1938, 1926		**Mn^{0}-L; L = exogenous ligand**	2012, 1935, 1920
Mn^{-1}-cat	1911, 1811		**Mn^{-1}-cat**	1911, 1810
Mn^{I}-H	1991, 1892, 1888		**Mn^{I}-H**	1990, 1892

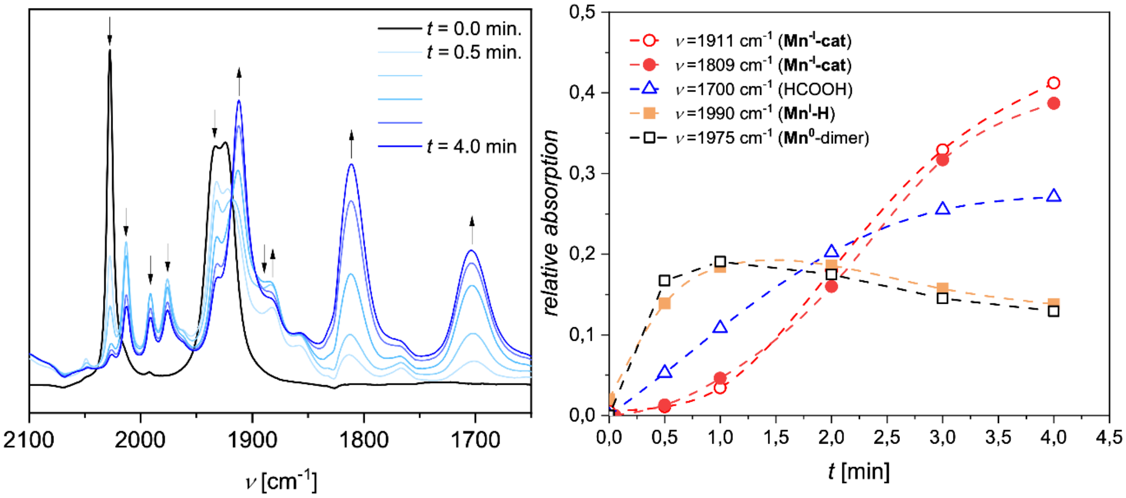

Fig. S17. Time-dependance of the IRSEC spectrum (*left*) for the **Mn^{I}-cat/Fe-S** (1:2) composite system under CO_2 in the presence of TFE (0.08 M) during CPE at -1.85 V (*light to deep blue*) and associated absorption profile variation (*right*). Note that at such a negative potential, slow formation of **Mn^{-1}-cat** can be expected but competes with the most favorable generation of **Mn^{I}-H**, as highlighted by the high intensity associated to the signals of **Mn^{I}-H** at short electrolysis time and the respectively low intensity of the signals associated to **Mn^{-1}-cat**. Nevertheless, catalysis at such negative potential is fast, and results in the fast consumption of the CO_2 and TFE substrates contained in the very small IR-SEC cell volume. Accordingly, **Mn^{-1}-cat** species accumulate in the cell over prolonged electrolysis period, as highlighted in the absorption profile above. The reduction is much favored while TFE is consumed, since the presence of TFE causes a shift of the reduction potential to **Mn^{-1}-cat** to more cathodic potentials (see Fig. S1, right).

3.1 General discussion on IRSEC results

The IR vibrations observed during the spectro-electrochemistry (SEC) measurements at various conditions were analysed with respect to previously reported values. **Fe-S** did not generate any noticeable change in the FTIR spectra within the vibration range of interest (2100 – 1600 cm^{-1}) upon application of the relevant potentials for this study, in the presence or absence of CO_2 and TFE. Similarly, in the case of the composite **Mn^{I}-cat/Fe-S** (1:2) system, no discernible changes in the IR-SEC spectra occurred at an applied potential of -1.3 V where the **Fe-S$^{0/-1}$** reduction occurred, besides the appearance of a small amount of the isomerized *mer*-**Mn^{I}-cat** species (2049, 1952 cm^{-1} *see* Fig. S13 and Table S5).[26]

Significant changes in the IRSEC spectra appeared for the **Mn^{I}-cat/Fe-S** (1:2) system at -1.65 V under CO_2 in the presence of 40 equiv. TFE (*blue spectra* in Fig. 2D and S14), where the gradual appearance of several new vibrations was observed over time (Fig. 2C). The final spectrum observed after 4 min electrolysis (Fig. 2D and S14-S16) showed vibrations at 1975, 1963, 1934, 1878 and 1853 cm^{-1} (*orange triangles*), indicative for the formation of **Mn^{0}-dimer**[27] yet in much lower amounts than in the IRSEC spectra obtained under identical conditions with **Mn^{I}-cat** (*orange and red spectra* in Fig. 2D and S14, respectively), as further highlighted in the difference spectra presented in Fig. S15. The additional vibrations (*blue stars*) observed in the presence of the **Mn^{I}-cat/Fe-S** (1:2) system at 1990 and 1892 cm^{-1} match well with the CO vibrations reported for the corresponding **Mn^{I}-H** species.[28,29] By comparison with other reported Mn^{I}-H vibrations,[30] the band at 1764 cm^{-1} was tentatively attributed to the corresponding metal-hydride bond vibration of the **Mn^{I}-H** species. This attribution was strengthened by the disappearance of this band when TFED was used instead of TFE while other CO vibrations attributed to **Mn^{I}-H** remained (Fig S15). Nevertheless, the Mn^{I}-D vibration, expected to appear in the 1250-1300 cm^{-1} range could not be observed as it lays in the vibrations of the acetonitrile solvent. The bands at 2012, 1935, 1920 cm^{-1} (*light blue pentagons*) were not observed before for such type of catalysts. The appearance of these vibrations was observed independently of the presence of TFE or CO_2. We reasoned that the hindered dimerization of **Mn^{I}-cat** observed in the presence of **Fe-S** could enable the generation of reduced monomeric species. Based on the fact that these stretches are significantly different from those of previously reported five coordinate monomeric Mn(0) species bearing a bulky substituted mesbpy ligand (6,6′-dimesityl-2,2′-bipyridine) (vibrations at 1984, 1894, 1880 cm^{-1})[31], but in good agreement with theoretically calculated values for the six-coordinated solvent bound Mn(0) species [Mn(pdbpy)$(CO)_3(CH_3CN)$], where pdbpy = 4-phenyl-6-(phenyl-2,6-diol)-2,2'-bipyridine (vibrations at 2014, 1938, 1926 cm^{-1})[29], we tentatively assigned these stretches to a similar neutral, hexacoordinated Mn(0) complex [Mn(bpy)$(CO)_3$L], **Mn^{0}-L** (L being an exogenous ligand, for example a MeCN molecule). A weak interaction between **Mn^{I}-cat** and **Fe-S^{-1}** might trigger the formation of such monomeric species. Last, no vibrations were observed in the 1680-1620 cm^{-1} range for the **Mn^{I}-cat/Fe-S** (1:2) mixture in the presence of CO_2 (Fig. S18), ruling out the formation of $[Mn^{I}\text{-}CO_2]^-$ species.[32,33] Formation of such species within the reaction mechanism was hence not considered.

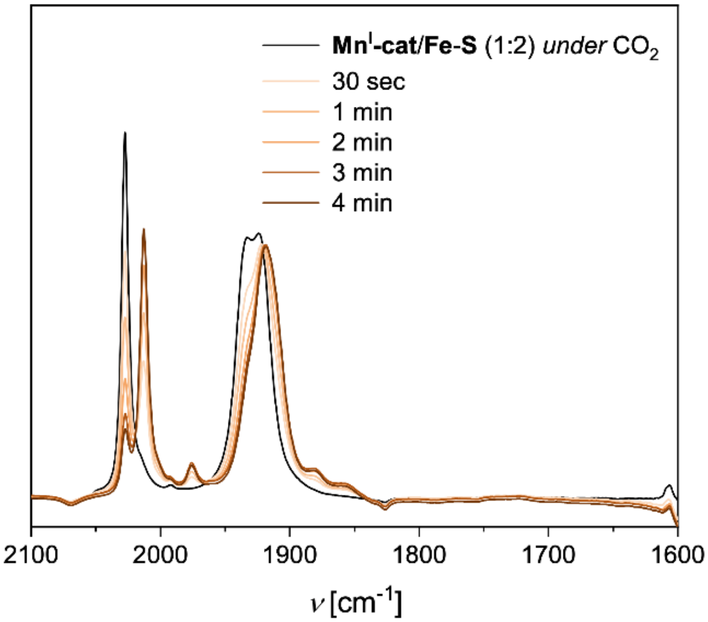

Fig. S18. Time dependent IRSEC data acquired for **Mn^{I}-cat/Fe-S** (1:2) in CO_2 saturated CH_3CN (0.1 M $TBAPF_6$) at -1.65 V.

4. NMR characterisation of the Mn-H species

NMR data were obtained in a series of *ex-situ* type experiments: a solution of 5 mM **Mn^{I}-cat** in 0.1 M $TBAPF_6$/CD_3CN (6 mL) was electrolysed using a glassy carbon plate working electrode (2 cm^2) and Pt wire (0.5 mm diameter, 10 cm length) as a counter electrode in a H-type CPE cell with its two compartments separated by two Ceramic-PVDF Composite membranes (16 µm thickness, Xuran) in an Ar-filled glovebox in the presence or the absence of 1 equiv. of **Fe-S** at the relevant potentials discussed below.

During this work, we observed that the non-aqueous Ag/$AgNO_3$ (10 mM in 0.1 M $TBAPF_6$/CH_3CN) reference electrodes used in our initial studies did not allow maintaining a stable potential over the course of the electrolysis and drifted towards more cathodic potentials, resulting in the appearance of over-reduced species (see discussion below on the optimisation of preparative electrolysis experiments of **Mn^{I}-cat** and **Fe-S** mixtures and stability of the species formed). We hence moved to aqueous Ag/AgCl (3 M KCl) electrodes, known to be significantly more stable over long electrolysis periods,[34] using a non-aqueous 0.1 M $TBAPF_6$/CH_3CN guard equipped with a Vycor® frit. When sealed appropriately, such electrodes can be used safely in a glovebox, and we strongly recommend their use instead of Ag/$AgNO_3$ reference electrodes when a constant potential should be maintained over a long electrolysis time.

The samples (~ 0.5 mL) were collected in a J-Young NMR tube when the current had decreased to less than ca. 5% of the current at the start of the electrolysis. The corresponding charges consumed over these electrolyses were in good agreement with the quantitative reduction of the 1 or 2 equiv. of the redox active species present in the solution (**Mn^I-cat** and **Fe-S**). 10 µL of TFE or 40 µL of a CO_2 purged 2 M TFE solution in 0.1 M $TBAPF_6/CD_3CN$ was then added to the NMR tube. The sample was immediately transferred to a salt-ice bath (-20 °C) prior to the transfer to the NMR spectrometer. The data were immediately collected in a pre-cooled probe (-20 °C). The portions of the spectra between ca. 5.5 and -2 ppm were omitted for clarity as this range contains the intense peaks of the tetrabutylammonium cation from the supporting electrolyte and as well as those of in excess added TFE. The signals for **Fe-S^{-1}**,[35] **Mn^I-H,**[36] **Mn^I-cat**, **Mn^0-dimer** and **Mn^{-1}-cat** were attributed according to the independent generation of these species following reported procedures.

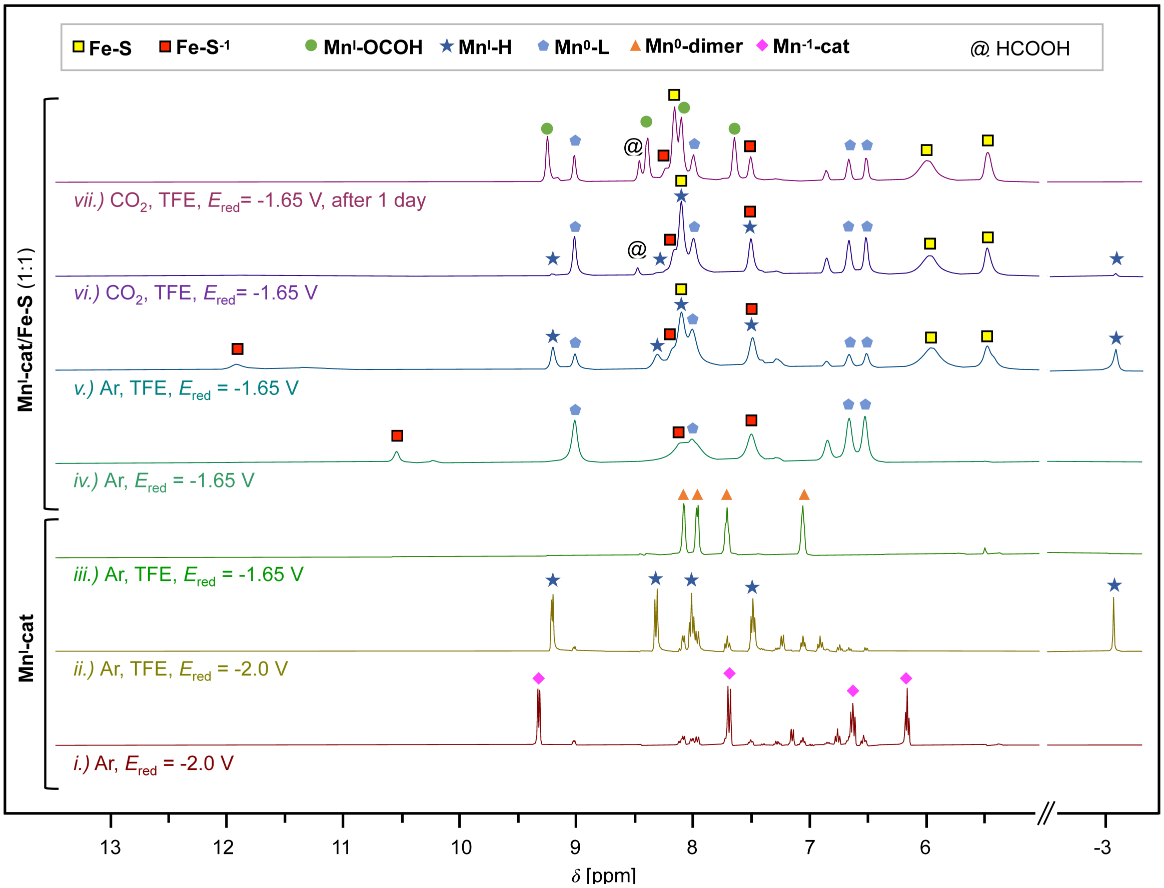

Fig. S19. Overlay of *ex-situ* ^{1}H NMR spectra in the presence and the absence of **Fe-S** at -20 °C. The spectrum in *brown* (*i.*) was obtained after electrolysis of **Mn^I-cat** at -2 V. The *olive* spectrum (*ii.*) was obtained after addition of 50 equiv. TFE to it. The *light green* spectrum (*iii.*) was obtained after reduction of **Mn^I-cat** at -1.65 V. The *teal* spectrum (*iv.*) was obtained after reduction at -1.65 V of a 1:1 **Mn^I-cat**/**Fe-S** solution. The spectrum in *blue* (*v.*) was observed after addition of 10 µL of TFE to the previous sample. The *dark violet* spectrum (*vi.*) was recorded immediately after addition of 30 µL of CO_2 purged 2 M TFE solution in CD_3CN to another 1:1 **Mn^I-cat**/**Fe-S** sample reduced at -1.65 V, and after 1 day in *purple* (*vii.*).

The ^{1}H NMR spectrum of a mixture of **Mn^{I}-cat/Fe-S** (1:1) in 0.1 M TBAPF$_6$/CD$_3$CN reduced by a CPE at -1.65 V, which was recorded immediately after the addition of a CO$_2$ saturated solution of CD$_3$CN containing TFE according to the procedure described above, revealed the formation of **Mn^{I}-H** (δ = 9.23, 8.27, 8.02, 7.48 and -3.12 ppm) along with the appearance of signals of **Fe-S** (δ = 8.10, 5.98, 5.44 ppm) and unreacted **Fe-S^{-1}** (δ = 10.52*, 8.08 and 7.47 ppm; *as previously reported,[35] we observed that this peak originating from the *m*-H of PhS$^-$ ligand may appear over a vast range of chemical shift, from ca. 10 to 25 ppm with broad peaks in the presence of proton sources or residual amounts of **Fe-S**, and is probably involved in redox and protonation exchange phenomena) (*green* spectrum in Fig. 2E, *dark violet* spectrum (*vii.*) in Fig. S19). The resonances at δ = 9.00, 7.98, 6.65, 6.50 ppm were tentatively assigned to the corresponding **Mn^{0}-L** species proposed in the IRSEC data analysis. The shift of the peaks assigned to **Mn^{0}-L** upon warming the NMR sample to 25 °C (Fig. S20) confirmed the paramagnetic nature of this species and the proposed assignment to a Mn(0) species. Interestingly, when the same experiment was repeated in the absence of **Fe-S**, the CPE step revealed the consumption of approx. one equivalent of electrons only, and the absence of **Mn^{I}-H** (*orange* spectrum in Fig. 2E, *light green* spectrum (*iii.*) in Fig. S19**)**. Under these conditions, **Mn^{0}-dimer** is the main species observed in solution, confirming that the generation of **Mn^{I}-H** is mediated at that potential by **Fe-S**. Note that the formation of **Mn^{I}-H** can be observed in the absence of **Fe-S**, but only when significantly more cathodic potentials are applied during the CPE step, enabling the formation of the doubly reduced **Mn^{-1}-cat** complex. This reduction occurs when applying a potential of -2 V during the CPE step, resulting in the consumption of 2 equiv. of charge to generate **Mn^{-1}-cat** (*δ* = 9.32, 7.67, 6.61, 6.12 ppm) (Fig. S19, *brown* spectrum (*i.*)). Addition of 50 equiv. of TFE to the same NMR tube gave rise to the spectra shown in *orange* (*ii.*) in Fig. S19, indicating the formation of **Mn^{I}-H**, in agreement with previous studies.

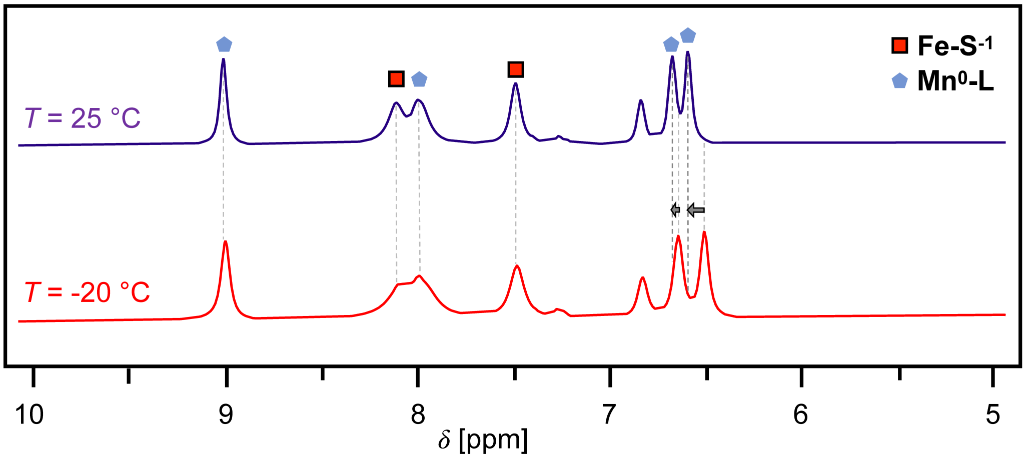

Fig. S20. ^{1}H NMR spectra collected after reduction at -1.65 V of a 1:1 **Mn^{I}-cat/Fe-S** solution measured at -20 °C (*red*) and 25 °C (*blue*).

It should be noted that observing the **Mn^{I}-H** species in such *ex-situ* studies in the presence of CO$_2$ is challenging as the catalytic hydride transfer to CO$_2$ makes the **Mn^{I}-H** species significantly more labile in solution. The catalytic activity of the hydride species is further highlighted by the presence of a formic acid peak (@ symbol in Fig. S19). This signal further increases over time, along with the decrease of the **Mn^{I}-H** peaks. The ^{1}H NMR spectrum after one day of the same **Mn^{I}-cat/Fe-S** (1:1) mixture in the presence of CO$_2$ and TFE reveals the full consumption of the **Mn^{I}-H** species together with an increase of the formic acid peak (Fig. S19*, purple* spectrum). Interestingly, formation of the corresponding **Mn^{I}-OCHO** species (δ = 9.24, 8.37, 8.14, 7.63 and 8.44 ppm)[36] is also observed under these conditions. Note that small amounts of **Fe-S^{-1}** and **Mn^{0}-L** were still detected in the ^{1}H NMR spectra after one day, which we attribute to the small driving force of the reaction of **Mn^{I}-H** with CO$_2$, anticipated from the low hydricity of the generated **Mn^{I}-H** species. The same reactivity towards CO$_2$ was observed for **Mn^{I}-H** generated as described above in the absence of **Fe-S** (Fig. S21).

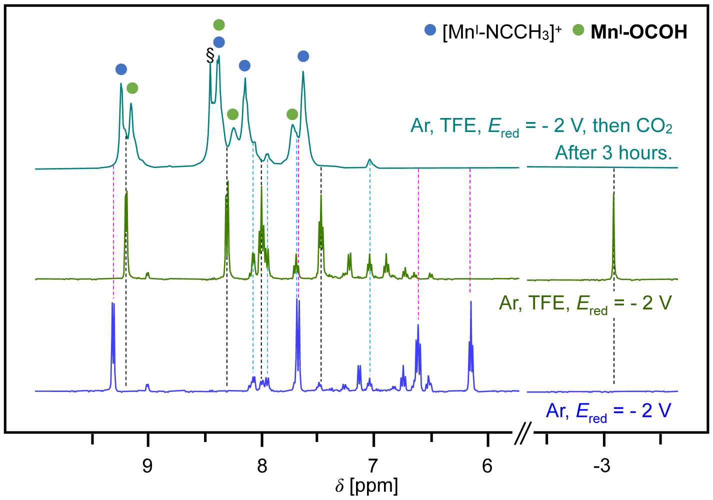

Fig. S21. Overlay of the ^{1}H NMR spectra recorded after electrolysis at -2 V of **Mn^{I}-cat** and subsequent addition of TFE and CO$_2$. The spectrum in *blue* was recorded immediately after electrolysis. The *green* spectrum was recorded after addition of TFE (10 µL) to that sample. The *light blue* spectrum was recorded 3 h after further addition of 20 µL of CO$_2$ purged CD$_3$CN to the previous sample. The ^{1}H NMR features of the [Mn^{I}-NCCH$_3$]$^{+}$ and **Mn^{I}-OCHO** complexes are attributed according to literature[1,36] and indicated with *blue* and *green* circles respectively. *§* indicates the peak for HCOOH/HCOO^{-}. The peaks for **Mn^{-1}-cat**, **Mn^{I}-H** and **Mn^{0}-dimer** species are labeled with *pink, black* and *light blue* dashed lines respectively.

The identity of the formic acid/formate peak at δ = 8.44 ppm was confirmed by carrying out the same experiment using TFED instead of TFE. Appearance of a peak at the same value in ^{2}H NMR confirmed the peak attribution (*purple* spectrum in Fig. S22).

In addition, to enable the formation of **Mn^{I}-H** in larger amounts in *ex-situ* studies, we carried out a similar experiment but in the absence of CO_2, to prevent the catalytic hydride consumption. The ^{1}H NMR spectrum of the 1:1 mixture of **Mn^{I}-cat**/**Fe-S,** electrolyzed at -1.65 V followed by the addition of 10 µL TFE according to the procedure described above is presented as the *blue* spectrum in Fig. 2E in main text and as the *blue* spectrum (*v.*) in Fig. S19. It reveals the formation of **Mn^{I}-H** in significantly larger amounts than in the presence of CO_2, as it is not consumed in the catalytic reaction. The appearance of a peak at -3.1 ppm in the corresponding ^{2}H NMR when the experiment was carried out in the presence of TFED instead of TFE unambiguously confirmed the formation and assignment of the **Mn^{I}-H** species (*light green* spectrum in Fig. S22)

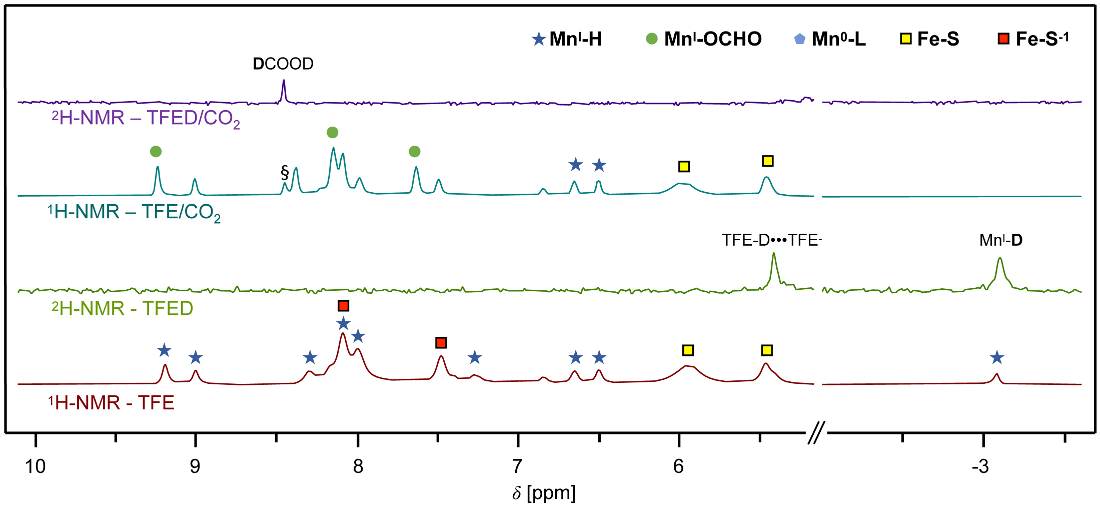

Fig. S22. Overlay of ^{1}H and ^{2}H-NMR spectra of the **Mn^{I}-H** species generated after reduction at -1.65 V of a 1:1 **Mn^{I}-cat**/**Fe-S** solution and addition of TFE (*brown*) or TFED (*green*) followed by CO_2 (*blue* and *purple* spectrum, respectively, recorded 1 day after CO_2 addition).

4.1 Optimisation of preparative electrolysis experiments of Mn^{I}-cat/Fe-S mixtures and stability of the electrochemically reduced species

As mentioned above, the use of Ag/$AgNO_3$ (10 mM in 0.1 M $TBAPF_6/CH_3CN$) reference electrode was found to be inappropriate for the preparative electroreduction of **Mn^{I}-cat**/**Fe-S** (1:1) mixtures. This reference electrode was found appropriate when using **Mn^{I}-cat** only, which showed very reproducible results by NMR upon preparative electrolysis in agreement with a gradual decrease of the electrolysis current over time, stabilizing at a minimal value (< 5% of the initial current), and the charge passed being consistent with the total charge expected from 1 equiv. (2.9 C when E_{red} = -1.65 V) or 2 equiv. (5.8 C when E_{red} = -2.0 V) of electrons transferred to **Mn^{I}-cat** (Fig. S23a).

However, a significantly different behavior was observed upon electrolysing **Mn^{I}-cat/Fe-S** (1:1) mixtures at -1.65 V using the same reference electrode. In that case, a gradual decay of the current was observed, but the current remained significant even at prolongated electrolysis periods (≥ 10% to the initial current after 3 h) and resulting in a total charge passed exceeding 1 equiv. of charge (> 5.8 C; Fig. S23b).

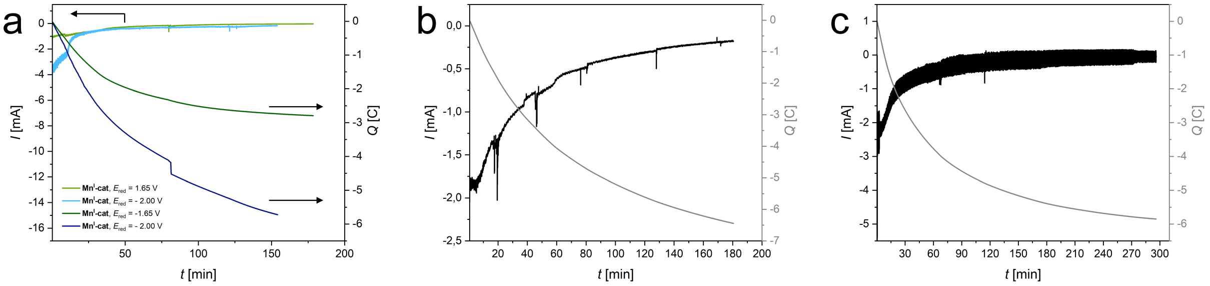

Fig. S23. Current *vs*. time plot and corresponding charge passed over the preparative electroreduction of (a) **Mn^{I}-cat** at -1.65 V and -2.00 V (Ag/AgNO$_3$ reference electrode), (b) **Mn^{I}-cat/Fe-S** (1:1) solution at -1.65 V (Ag/AgNO$_3$ reference electrode) and (c) **Mn^{I}-cat/Fe-S** (1:1) solution at -1.65 V (Ag/AgCl reference electrode).

The ^{1}H NMR analysis of this electrolysed solution over increasing charge passed showed the gradual disappearance of the features for **Mn^{I}-cat** and **Fe-S** and the gradual appearance of two new sets of peaks attributed to **Fe-S^{-1}** and **Mn^{0}-L**, as reported above using a Ag/AgNO$_3$ reference electrode (Fig. S24, *brown* to *blue* spectrum). However, at prolonged electrolysis time and higher amount of charge passed (> 1 equiv. of charge), the intensity of the signals of **Mn^{0}-L** decreased concomitantly with the appearance of the peaks assigned to **Mn^{-I}-cat** (*pink* diamonds, *blue* spectrum in Fig. S24). Suspecting a potential drift of the Ag/AgNO$_3$ reference electrode value over prolonged electrolysis time in the presence of **Fe-S**, we moved towards more stable Ag/AgCl (3M KCl) reference electrodes, as highlighted in the previous section. A markedly different current variation was observed, as the current stabilized rapidly to a low current value (< 5% of the initial current) while only a maximum of 1 equiv. charge could be passed even at prolonged electrolysis time (over 4 h, Fig. S23). Concomitantly, no peak assigned to **Mn^{-I}-cat** could be observed in the ^{1}H NMR spectrum (Fig. S25).

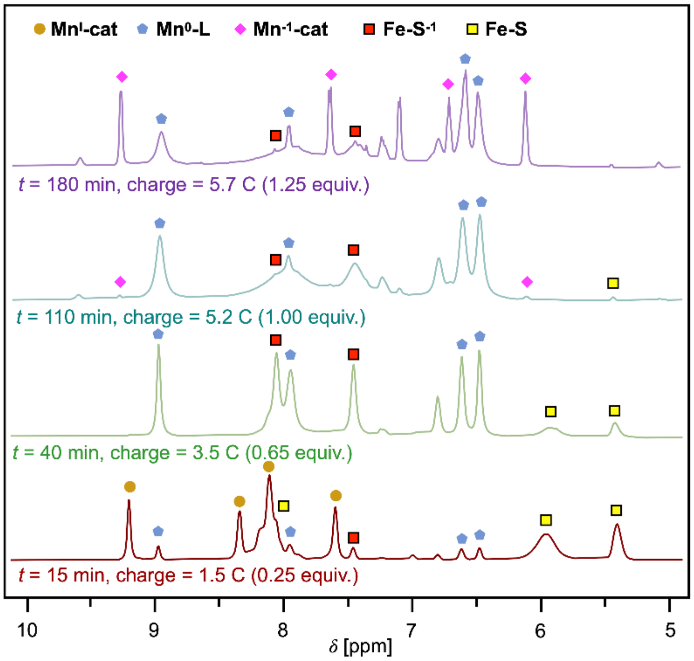

Fig. S24. Overlay of *ex-situ* ^{1}H NMR spectra recorded at -20 °C, after electrolysis at -1.65 V of **Mn$^{\mathrm{I}}$-cat/Fe-S** (1:1) solution using Ag/AgNO$_3$ as reference electrode. The spectra in *brown* was obtained after 15 min, the *green* spectrum after 40 min, the *blue* spectrum after 110 min and the *purple* spectrum after 180 min of CPE.

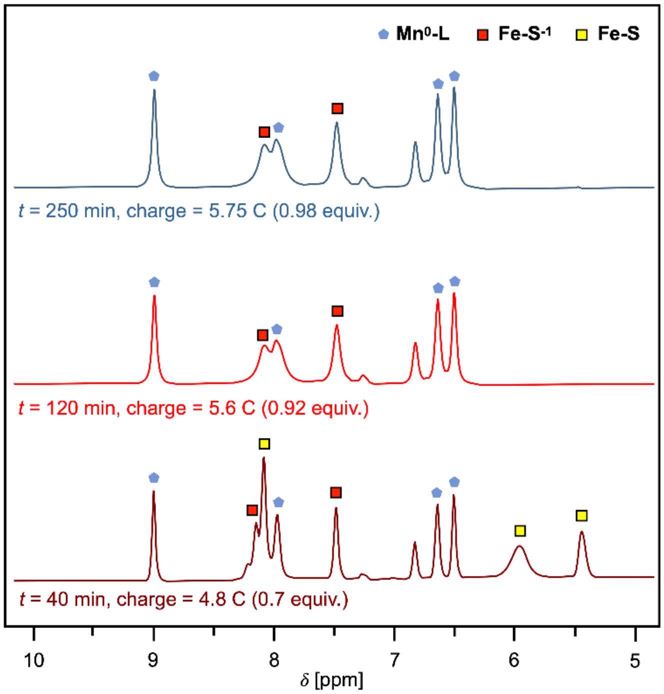

Fig. S25 Overlay of *ex-situ* ^{1}H NMR spectra recorded at -20 °C, after electrolysis at -1.65 V of a **Mn$^{\mathrm{I}}$-cat/Fe-S** (1:1) solution using Ag/AgCl as reference electrode. The spectra in *brown* was obtained after 40 min, the *red* spectrum after 120 min and the *blue* spectrum after 150 min of CPE.

Last, to rule out the formation of **Mn^{-1}-cat** by disproportionation of the **Mn^{0}-L** species generated during the preparative electrolysis experiments, the NMR sample collected in the procedure described above after 120 min of electrolysis (*red* spectrum in Fig. S25) was analysed by ^{1}H NMR over several hours (Fig. S26). The signals attributed to **Mn^{0}-L** stayed unchanged over time, ruling out a disproportionation to **Mn^{-1}-cat** at the experiment timescale.

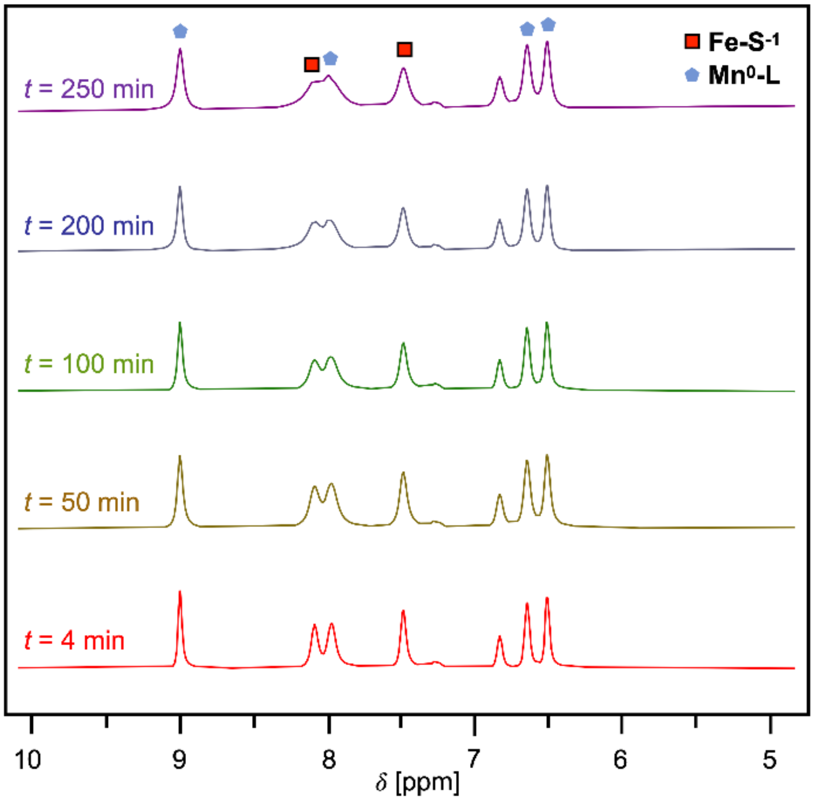

Fig. S26. Overlay of ^{1}H NMR spectra recorded at -20 °C, after electrolysis at -1.65 V of a **Mn^{I}-cat/Fe-S** (1:1) solution using Ag/AgCl as reference electrode 4 min (*red*), 50 min (*olive*), 100 min (*green*), 200 min (*blue*) and 250 min (*purple*) after electrolysis .The slight broadening of the signals over time can be attributed to a small drift of the NMR spectrometer shim over prolonged experimental time at low temperature.

5. H/D Kinetic Isotope Effect determination

In the absence of a clear 'S' shaped regime in the electrocatalytic cyclic voltammetry studies, typically used to estimate kinetic isotope effect (KIE) of a such an electrocatalytic system, we determined the kinetic isotope effect from the respective amount of formic acid generated in CPE experiments carried out with TFE and TFED, as these are proportional to the rate of the respective reactions. We hence performed a batch of CPE at -1.85 V with Mn^I-cat/Fe-S (1:2) solution under CO_2 using TFE and TFED as proton sources (0.2M) over 90 min. Subsequent product analysis enabled determining a KIE of 1.85 (Table S6). This KIE appears to be higher than that observed with an analogous Mn complex bearing proton relays in the vicinity of the Mn center and reacting via a PTET mechanism (KIE = 1.4).[28] Such a PTET mechanism is expected to display a lower KIE than the related CPET one, and the higher value determined here is in agreement with that hypothesis.

Table S6: Product analysis after 90 minutes CPE at -1.85 V in presence of a **Mn^I-cat/Fe-S** (1:2) solution. The CPEs were performed in the presence of 0.2 M TFE/TFED.

H^+/D^+ source	Charge [C]	Formic acid (D) [µmol]	CO [µmol]	KIE
TFE	5.7454	22.78	3.12	1.85
TFED	3.744	12.26	1.724	

6. Relative reaction rates of Mn^{-1}-cat with CO$_2$ and H$^+$

To rule out the formation of **Mn^{I}-H** in the catalytic conditions from **Mn^{I}-cat** via a ET-ET-PT process, generating **Mn^{-1}-cat** prior to its protonation, we carried out a kinetic analysis of the relative reaction rates of both substrates of the reaction (H$^+$ and CO$_2$) with **Mn^{-1}-cat**. Reaction of the isolated [K(18-crown-6)]**[Mn^{-1}-cat]** complex with CO$_2$ and a proton source was monitored by UV-Vis spectroscopy. We choose here *para*-chloro-phenol (pK_a = 25) as a proton source to model the apparent pK$_a$ of the solution in catalytic conditions, (a pK$_a$ value of 25.1 was proposed for CO$_2$-saturated TFE solutions in CH$_3$CN[14]). **Mn^{-1}-cat** shows a strong absorbance at 562 nm (ε = 8400 M^{-1}cm^{-1}), and reaction kinetics were evaluated by optically monitoring the decay of that band as a function of time. The pseudo-first order decay of this band was monitored with time in 20 mM solutions of the respective substrates (Fig. S27).

The results highlighted in the inset of Fig. S27c highlight that the relative reaction rate of **Mn^{-1}-cat** with CO$_2$ is at least 15 times faster than the one of with *para*-chloro-phenol, excluding a ET-ET-PT pathway in the catalytic conditions to generate **Mn^{I}-H** and confirming the CPET from **Fe-S^{-1}** and a proton donor to **Mn^{0}-L** to produce **Mn^{I}-H**. The detailed experimental procedure is provided below.

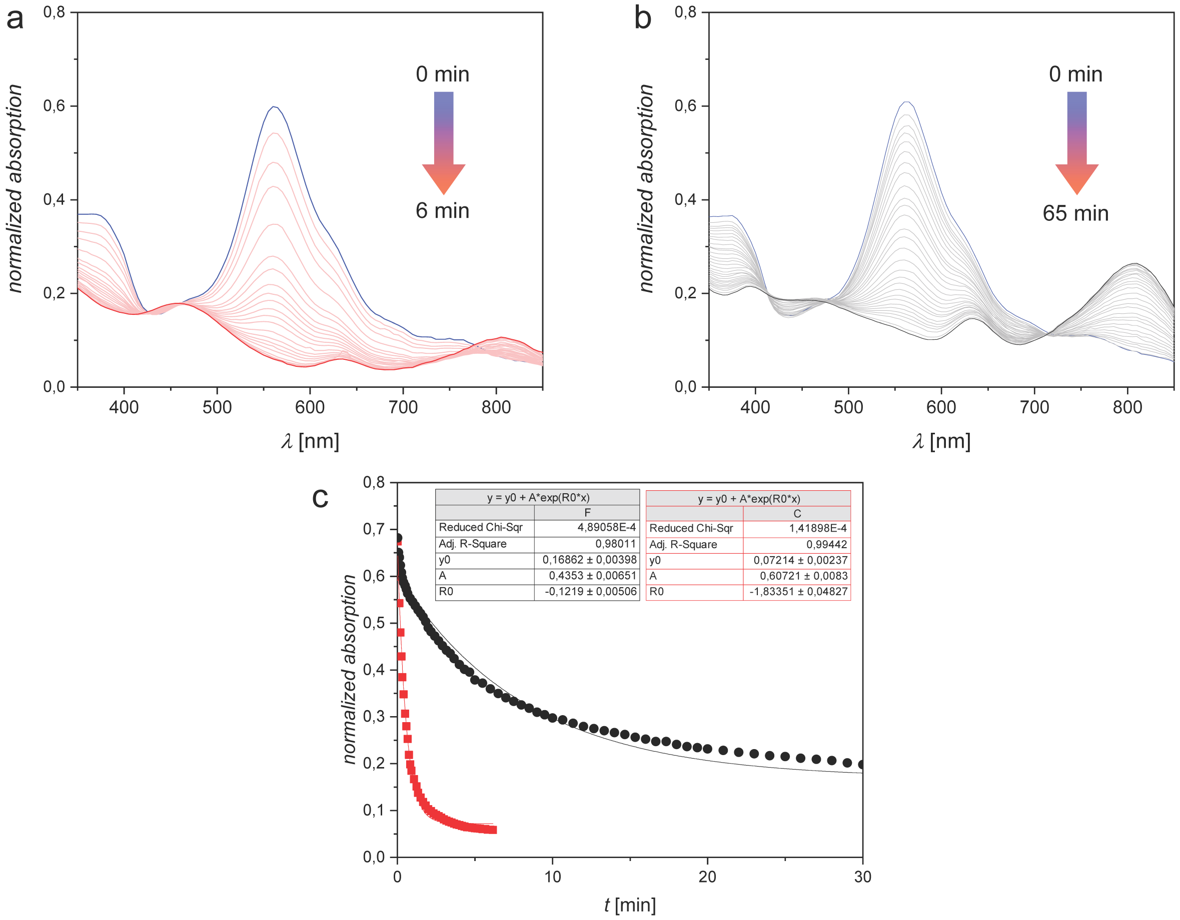

y = y0 + A*exp(R0*x)	
	F
Reduced Chi-Sqr	4,89058E-4
Adj. R-Square	0,98011
y0	0,16862 ± 0,00398
A	0,4353 ± 0,00651
R0	-0,1219 ± 0,00506

y = y0 + A*exp(R0*x)	
	C
Reduced Chi-Sqr	1,41898E-4
Adj. R-Square	0,99442
y0	0,07214 ± 0,00237
A	0,60721 ± 0,0083
R0	-1,83351 ± 0,04827

Fig. S27. UV-Vis spectra variation over time for 0.08 mM **Mn^{-1}-cat** complex and 20 mM CO$_2$ (a) or 20 mM 4-Cl-PhOH (b). (c) Absorbance at 560 nm vs. time for the spectra (a) (*red*) and (b) (*black*).

Experimental procedure.

CO$_2$ substrate: 180 µL of a CO$_2$-saturated CH$_3$CN solution (0.28 M CO$_2$ conc.) was mixed with 2.12 mL of an Ar-saturated CH$_3$CN solution in an air-tight UV-Vis cuvette, and a baseline was recorded. At t = 0 min, 200 µL of 1 mM Na(18-crown-6)[**Mn^{-1}-cat]** solution in CH$_3$CN was injected to the cuvette under stirring using a gas tight syringe.

4-Cl-PhOH substrate: 500 µL of a 100 mM solution of 4-Cl-PhOH in CH$_3$CN was mixed with 1.8 mL of a Ar-saturated CH$_3$CN solution in an air-tight UV-Vis cuvette, and a baseline was recorded. At t = 0 min, 200 µL of 1 mM Na(18-crown-6)[**Mn^{-1}-cat]** solution in CH$_3$CN was injected to the cuvette under stirring using a gas tight syringe.

7. Determination of pK_a and BDFE of Fe-S

The determination of the BDFE of **Fe-S** is not straightforward due to the possibility of side phenomena, in particular the hydrolysis of the thiolate ligands in CH_3CN solvent in the presence of strong acid sources. On that basis, and considering expected pK_a values, we chose the acid form of P1 type phosphazene base, *tert*-butylimino-tris(pyrrolidino)phosphorene (**P1.H$^+$**) (pK_a = 28.35 in CH_3CN), to protonate the reduced **Fe-S^{-1}** complex without hydrolyzing the thiophenolate ligands. A set of CV was recorded of **Fe-S** in the presence of various amounts of **P1.H$^+$**. A gradual positive shift of the **Fe-S**$^{0/-1}$ redox event was observed, while the reversible Nernstian wave shape is preserved (Fig. S28). Assuming a fast proton transfer rate, the following EC type reaction can be proposed:

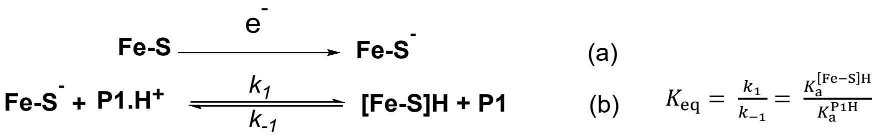

In such a reaction scheme the shift of the redox process induced by the EC mechanism can be used to determine the equilibrium constant of the EC process[37]:

$$E'_{\mathrm{p}} = E^0_{1/2} + \frac{RTln(1+K_{\mathrm{EC}})}{F} \quad \text{(xv)}$$

where, $E_p{}'$ is the apparent redox potential of the **Fe-S$^{0/-1}$** process in the presence of the proton source. As pseudo first order reaction kinetics can be expected for the protonation, the overall rate of the C step will be dependent of the ratio of **Fe-S** and **P1.H$^+$** and the equation (xv) can be expressed as [37]

$$E'_{1/2} = E^0_{1/2} + \frac{RTln(1+K_{\mathrm{eq}}\frac{[\mathbf{P1.H^+}]}{[\mathbf{Fe\text{-}S}]})}{F} \qquad \text{(xvi)}$$

Accordingly,

$$\left(1 + K_{\mathrm{eq}}\frac{[\mathbf{P1.H^+}]}{[\mathbf{Fe\text{-}S}]}\right) = e^{F/RT(E'_{1/2}-E^0_{1/2})} \qquad \text{(xvii)}$$

A plot of $e^{F/RT(E'_{1/2}-E^0_{1/2})}$ *vs*. **[P1.H$^+$]/[Fe-S]**, using the potential values obtained from the CV experiments at various **P1.H$^+$** concentrations, presented in Fig. S25 allows determining K_{eq}, being the slope value. We hence determined that $\boldsymbol{K_{\mathrm{eq}}}$ **= 77 ± 2**.

As K_{eq} is the ratio of the K_a values of **[Fe-S]H** and **P1.H$^+$**, the pK_a value of **[Fe-S]H** can be determined as:

$$\mathrm{p}K_a^{[\mathrm{Fe\text{-}S}]\mathrm{H}} = \log(K_{\mathrm{eq}}) + \mathrm{p}K_a^{\mathrm{P1.H^+}} \qquad \text{(xviii)}$$

Hence, p$K_a^{[\mathrm{Fe\text{-}S}]\mathrm{H}}$ **= 30.2 ± 0.3.**

Utilizing this pK_a value and the redox potential determined via CV for **Fe-S** allowed us to determine $\mathrm{BDFE}^{\mathbf{Fe\text{-}S}}$ using the Bordwell equation (3) as presented in Figure 3 in main text so that:

$$\mathrm{BDFE}^{\mathbf{Fe\text{-}S}} = \mathbf{63.5 \pm 0.8\ kcal/mol}$$

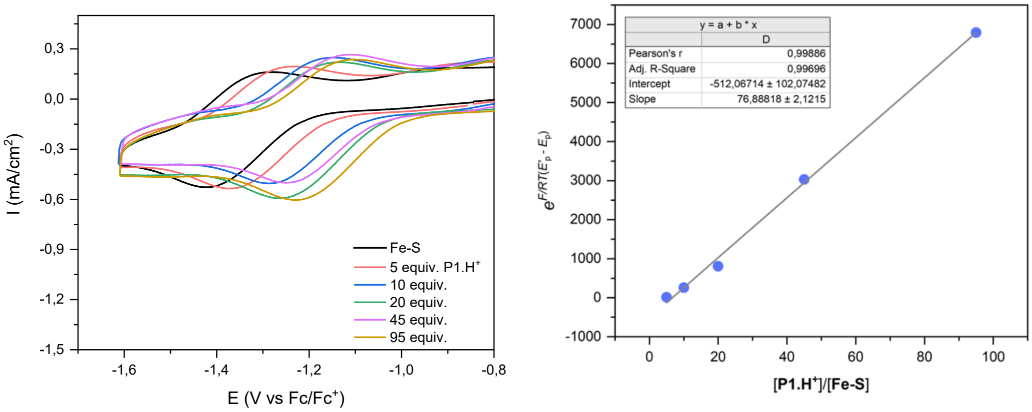

Fig. S28. (*left*) CVs of **Fe-S** recorded in the presence of increasing amounts of **P1.H**$^+$ in 0.1 M TBAPF$_6$/CH$_3$CN (500 mV·s^{-1} scan rates). (*right*) Corresponding $e^{F/RT(E'_{1/2}-E^0_{1/2})}$ *vs.* $\frac{[\mathbf{P1.H}^+]}{[\mathbf{Fe\text{-}S}]}$ plot to determine K_{eq}. The linear regression fit has a slope of 77 ± 2 with $R^2 = 0.997$.

8. Estimation of BDFE of $\mathbf{Mn^{I}}$-H

To estimate the $\mathrm{BDFE}^{\mathbf{Mn^{I}\text{-}H}}$ of the $\mathbf{Mn^{I}}$**-H** species using the Bordwell equation introduced in main text, we established a thermochemical cycle for its generation, shown below in Fig. S29. We considered here the ET-PT step of the proposed cycle for calculation.

In the ET step, the accurate determination of the redox potential for the reduction of monomeric $\mathbf{Mn^{0}}$**-cat** to monomeric $\mathbf{Mn^{-1}}$**-cat,** $E^{0/-1}_{\mathbf{Mn^0-cat}}$, is complex, as $\mathbf{Mn^{0}}$**-cat** is unstable in solution and undergoes fast dimerization to generate the more stable $\mathbf{Mn^{0}}$**-dimer**. Hence, the redox potential of the reduction of $\mathbf{Mn^{0}}$**-dimer** to $\mathbf{Mn^{-1}}$**-cat** will occur at a more cathodic potential than the one required to reduce or oxidize the monomeric $\mathbf{Mn^{0}}$**-cat**. This is in agreement with the fact that when dimerization is hindered, the second electron transfer to generate the Mn(-I) species is more favorable than the initial reduction to the Mn(0) species, resulting in two electron transfer steps occurring at the potential required for the first reduction.[11] Nonetheless, one electron oxidation potential of $\mathbf{Mn^{-1}}$**-cat** was recently determined to be -1.48 V[36] and was hence used here to determine the lower boundary of $\mathrm{BDFE}^{\mathbf{Mn^{I}\text{-}H}}$.

In the PT step, the pK_a of $\mathbf{Mn^{I}}$**-H** species can be estimated from the ^{1}H NMR data shown in Fig. S19 (*brown* (*i.*) and *olive* (*ii.*) spectra): addition of 50 equiv. of TFE to $\mathbf{Mn^{-1}}$**-cat** led to the quantitative generation of corresponding $\mathbf{Mn^{I}}$**-H**. Considering the pK_a value of 34 for TFE in CH_3CN, this indicates that the pK_a of the $\mathbf{Mn^{I}}$**-H** has to be ≥ 34.

The values proposed above for the ET-PT steps hence allow to calculate the lower limit of $\mathrm{BDFE}^{\mathbf{Mn^{I}\text{-}H}}$ according to the Bordwell equation:

$$\mathrm{BDFE}^{\mathbf{Mn^{I}\text{-}H}} \geq 23.06 \times (-1.48) + 1.364 \times 34 + 53.6\ \mathrm{kcal/mol}$$

$$\mathrm{BDFE}^{\mathbf{Mn^{I}\text{-}H}} \geq 65.8\ \mathrm{kcal/mol}$$

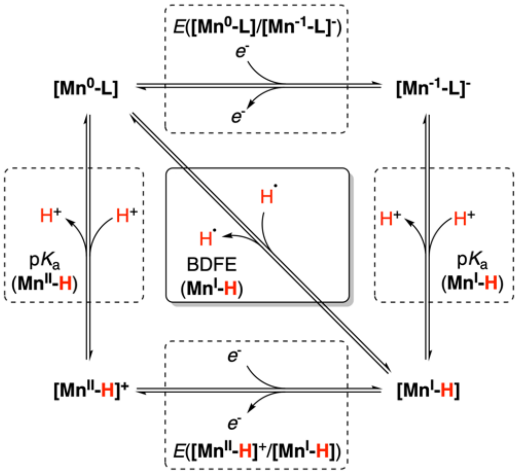

Fig. S29. Proposed thermochemical cycle for the formation of $\mathbf{Mn^{I}}$**-H**.

9. CO_2RR activity of Mn^I-cat in the presence of other CPET mediators

We investigated here the CO_2RR activity of **Mn^I-cat** in the presence of $[Ru^{III}(acac)_2(PyImz)][OTf]$ (**[Ru-NH$^+$]**[OTf]) [that can *in situ* generated by electrochemical reduction of the actual CPET donor $[Ru^{II}(acac)_2(PyImz)]$ **(Ru-NH)** (BDFE = 62 kcal/mol),[4] **DTH_2Q** (BDFE = 62.9 kcal/mol)[38], **H_2Q** (BDFE = 67.3 kcal/mol)[38] and PhOH (BDFE = 88 kcal/mol).[39]

The CV of the 1:1 **Mn^I-cat**/**Ru-NH** composite system showed only a slight current enhancement of the process at -1.85 V when TFE was used as proton source (Fig. S30 *left*). A CPE at -1.85 V under CO_2 under these conditions (0.2 M TFE) led to the determination of FYs of 63 ± 4% for CO and 35 ± 6% for HCOOH (Table S7 entry 1). A significant enhancement of the peak at -1.85 V was observed when using H_2O instead of TFE as a proton source (Fig. S30 *right*). This strong current enhancement prompted us to investigate the selectivity for CO_2RR at -1.85 V in the presence of water (1.5 M), revealing a FY of 62 ± 7% for HCOOH, 24 ± 2% for CO and~2% for H_2 (Table S7 entry 5). The higher selectivity for HCOOH observed here in the presence of H_2O as well as the multiple turnovers can be explained by the need of a stronger acid than TFE to regenerate **Ru-NH**: the *in situ* generated H_2CO_3 in the presence of H_2O and CO_2 (pK_a of H_2CO_3 = 17.03 in CH_3CN) is acidic enough to protonate the corresponding base **Ru-N$^-$** (pK_a(**Ru-NH**) = 22.1 in CH_3CN),[4] at the difference of compared to TFE (pK_a = 25.1 in the presence of CO_2 in CH_3CN). The shift of the **Ru-NH$^{+/0}$** reduction potential observed in Fig. S30, *right*, further highlights the occurrence of such a PCET mechanism in the presence of H_2O. However, the appearance of H_2 as a minor reaction product (FY_{H2} = 2%, Table S1) suggests that protonation of the Mn hydride species occurs in presence of this stronger acid. Analogously, FY for H_2 over 50%[36] and 20%[40] were recently reported for **Mn^I-cat** when using morpholine in presence of CO_2 ($pK_a \approx 17$) and Et_3NH^+ (pK_a = 18.3) as proton sources, respectively. This further illustrates the importance of avoiding the use of proton sources with lower pK_a values to maintain high selectivity against undesired H_2 evolution.

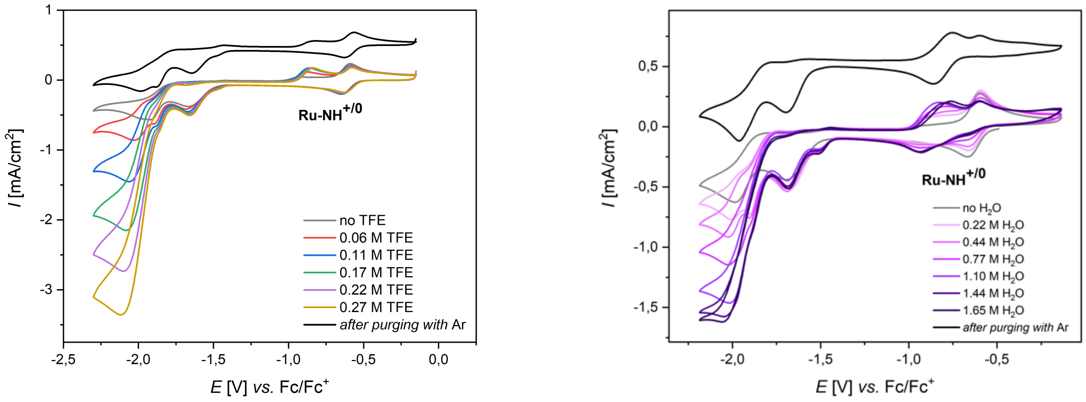

Fig. S30. (*left*) Overlay of the CVs of **Mn^{I}-cat/Ru-NH** (1:1) under CO_2 with incremental addition of TFE and after removal of CO_2. (*right*) Overlay of CVs of **Mn^{I}-cat/Ru-NH** (1:1) mixtures under CO_2 with incremental addition of H_2O as well as after removal of CO_2.

In the presence of the fully organic hydrogen atom donors such as **DTH$_2$Q**, **H$_2$Q** and PhOH, no additional proton source was added but an excess of the donor was used. The CVs for **Mn^{I}-cat** in the presence of **DTH$_2$Q**, **H$_2$Q** and PhOH were hence recorded respectively using 110:1, 500:1 and 100:1 ratio, with respect to **Mn^{I}-cat**. In the presence of PhOH**,** the CO_2RR activity showed the typical behavior reported for **Mn^{I}-cat**, *i.e.* a significant current enhancement was observed at ca. -2.05 V and no catalytic wave at -1.85 V was observed (*sky blue trace* in Fig. S30 *left*).[10] Accordingly, CPE carried out in the presence of PhOH revealed the formation of CO as the sole CO_2RR product with high FY (87 ± 3%) (Table S7 entry 4) . Similar catalytic behavior was observed in the presence of **H$_2$Q** with CO being the sole CO_2RR product, yet with substantially higher current enhancement in the CV (Fig. S31 *right*) and a ca. three-fold enhancement in CO_2RR activity with respect to that observed with PhOH (Table S7, entry 3).

DTH$_2$Q demonstrated a markedly different behavior: the CV recorded for **Mn^{I}-cat** under CO_2 and in the presence of **DTH$_2$Q** presented a clear redox process at -1.85 V (*green trace* in Fig. S31 *left*). Similar, to the other mediators displaying that redox feature, substantial amounts of HCOOH were detected in the corresponding CPE experiment (FY_{HCOOH} = 67±8%, FY_{CO} = 27±2%, Table S7, entry 2), highlighting the ability of **DTH$_2$Q** to quantitively generate **Mn^{I}-H**. Nevertheless, our attempts to use **DTH$_2$Q** in electrolytic HCOOH production were ineffective even in presence of H_2O as its pK_a (6.04 in H_2O) is predicted to be significantly lower [41] compared to *in situ* generated H_2CO_3 (17.03). We conjectured that the slow reaction rates and moderate TONs of **DTH$_2$Q** results from kinetic limitations arising from its high steric bulk, that in a Marcus normal region can be translated into an increased donor-acceptor distance lowering both rates for CPET transfer and regeneration at the electrode.

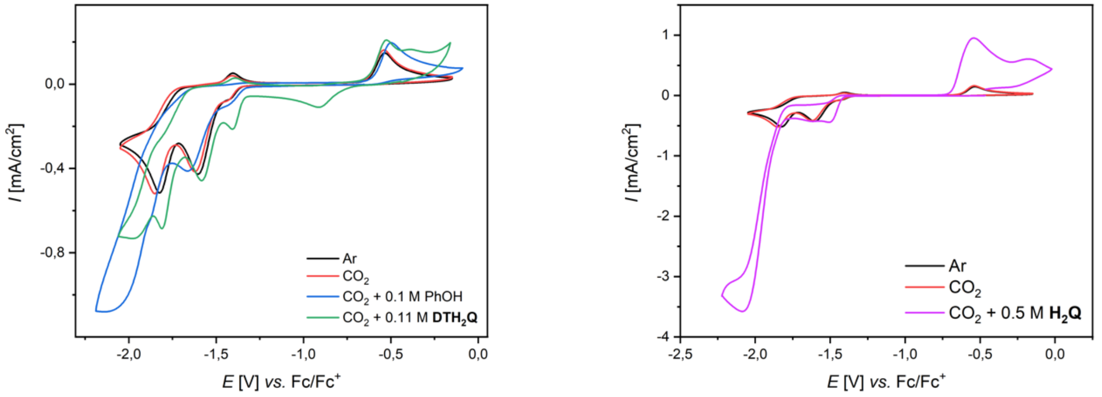

Fig. S31. (*left*) Overlay of the CVs of **Mn^{I}-cat** under Ar (*black*), CO_2 (*red*) and after subsequent addition of 0.11 M **DTH$_2$Q** to the CO_2 saturated solution (*green*). The reduction event at -0.8 V is originating from the corresponding benzoquinone impurity that could not be removed even after purification. The concentration of **DTH$_2$Q** is limited by the highest concentration that can be achieved in 0.1 M $TBAPF_6/CH_3CN$. The *blue* trace corresponds to the CV of **Mn^{I}-cat** recorded in the presence of 0.1 M PhOH. (*right*) Overlay of the CV features for **Mn^{I}-cat** observed under Ar (*black*), CO_2 (*red*) and in the presence of 0.5 M **H$_2$Q** under CO_2 (*magenta*).

Table S7. Product analysis after 90 min CPE of **Mn^{I}-cat** in the presence of different CPET mediators and proton sources.

Entry	CPET mediator	H^+ source	Q_{CPE} [C]	Products formed [µmol]			FY (%)			
				CO	HCOOH	H_2	CO	HCOOH	H_2	Total
1[a]	**Ru-NH** (1 mM)	TFE (0.2 M)	3.28	10.69	4.95	-	63.2	34.5	-	97.7
2	**DTH$_2$Q** (0.11 M)	-	2.25	3.255	5.69	-	27	67	-	94
3	**H$_2$Q** (0.5 M)	-	8.34	32.68	-	0.5	78.8	-	1.5	80.3
4	**PhOH** (0.5 M)	-	3.02	13.88	-	-	86.6	-	-	86.6
5[a]	**Ru-NH** (1 mM)	H_2O (1.5 M)	5.44	5.24	13.813	0.44	23.5	62	1.8	87.3

[a] **Ru-NH** was generated *in-situ* by electrochemical reduction of [**RuNH$^+$**][OTf].

10. Hydricity of Mn^{I}-H

The hydricity (G_{H^-}) of **Mn^{I}-H** is determined from the thermochemical cycle of the overall reaction[12]

$$\mathbf{Mn^{I}\text{-}H} \rightarrow \mathrm{Mn}^0 + \mathrm{H}^\bullet \qquad \mathrm{BDFE} \qquad \text{(xix)}$$

$$\mathrm{Mn}^0 \rightarrow \mathrm{Mn}^+ + \mathrm{e}^- \qquad \mathrm{FE}^0_{\mathbf{Mn}^{+/0}} \qquad \text{(xx)}$$

$$\mathrm{H}^\bullet + e^- \rightarrow \mathrm{H}^- \qquad \Delta G_{\mathrm{H}^\bullet/\mathrm{H}^-} \qquad \text{(xxi)}$$

$$\mathbf{Mn^{I}\text{-}H} \rightarrow \mathrm{Mn}^+ + \mathrm{H}^- \qquad G^0_{\mathrm{H}^-} \qquad \text{(xxii)}$$

$$G^0_{\mathrm{H}^-} = \mathrm{BDFE} + \mathrm{F}E^0_{\mathrm{Mn}^{+/0}} + \Delta G_{\mathrm{H}^\bullet/\mathrm{H}^-} \qquad \text{(xxiii)}$$

where $E^0_{\mathrm{Mn}^{+/0}}$ is the reduction potential *vs.* Fc/Fc$^+$ of Mn$^{+/0}$ reduction that was determined to be -1.48 V by Saouma *et. al.*[36] In this work, we determined the lower limit of $\mathrm{BDFE}^{\mathbf{Mn^{I}\text{-}H}}$ to be 65.8 kcal/mol. We chose that lowest value for calculation as this will result in the lowest value of hydricity, in line with our goal of determining the thermodynamic feasibility of the hydride transfer to CO_2 ($G_{\mathrm{H}^-}^{\mathrm{HCOOH}} = 44\ \mathrm{kcal/mol}$). The free energy of the reduction of a hydrogen atom ($\Delta G_{\mathrm{H}^\bullet/\mathrm{H}^-}$) in CH_3CN is known to be 26 kcal/mol.[42]

The lowest estimation for G_{H^-} can hence be determined according to equation (xxiii):

$$G^0_{\mathrm{H}^-} \geq 57.6\ \ \mathrm{kcal/mol}$$

This value is in relatively good agreement with the value of 50.7(±1.1) kcal/mol recently determined by Saouma *et. al.*[36] We assume that the small deviation between these determined hydricity values may originate from small uncertainties in the determination of the pK_a values for **Mn$^{\mathbf{I}}$-H**.

Supplementary References

1 Bourrez, M., Molton, F., Chardon-Noblat, S. & Deronzier, A. [Mn(bipyridyl)$(CO)_3$Br]: an abundant metal carbonyl complex as efficient electrocatalyst for CO_2 reduction. *Angew. Chem. Int. Ed.* **50**, 9903-9906, doi:10.1002/anie.201103616 (2011).

2 Hagen, K. S., Reynolds, J. G. & Holm, R. H. Definition of reaction sequences resulting in self-assembly of $[Fe_4S_4(SR)_4]^{2-}$ clusters from simple reactants. *J. Am. Chem. Soc.* **103**, 4054-4063, doi:10.1021/ja00404a013 (1981).

3 Voss, M. E., Beer, C. M., Mitchell, S. A., Blomgren, P. A. & Zhichkin, P. E. A simple and convenient one-pot method for the preparation of heteroaryl-2-imidazoles from nitriles. *Tetrahedron* **64**, 645-651, doi:10.1016/j.tet.2007.11.009 (2008).

4 Wu, A., Masland, J., Swartz, R. D., Kaminsky, W. & Mayer, J. M. Synthesis and Characterization of Ruthenium Bis(β-diketonato) Pyridine-Imidazole Complexes for Hydrogen Atom Transfer. *Inorg. Chem.* **46**, 11190-11201, doi:10.1021/ic7015726 (2007).

5 Wang, B., Graskemper, J. W., Qin, L. & DiMagno, S. G. Regiospecific Reductive Elimination from Diaryliodonium Salts. *Angew. Chem. Int. Ed.* **49**, 4079-4083, doi:10.1002/anie.201000695 (2010).

6 Matson, B. D., McLoughlin, E. A., Armstrong, K. C., Waymouth, R. M. & Sarangi, R. Effect of Redox Active Ligands on the Electrochemical Properties of Manganese Tricarbonyl Complexes. *Inorg. Chem.* **58**, 7453-7465, doi:10.1021/acs.inorgchem.9b00652 (2019).

7 Murata, T., Hiyoshi, M., Ratanasak, M., Hasegawa, J.-y. & Ema, T. Synthesis of silyl formates, formamides, and aldehydes via solvent-free organocatalytic hydrosilylation of CO_2. *Chem. Commun.* **56**, 5783-5786, doi:10.1039/D0CC01371D (2020).

8 Alexandrova, A. V. *et al.* Synthesis of Electron-Rich Sterically Hindered P1 Phosphazene Bases by the Staudinger Reaction. *Eur J Org Chem* **2013**, 1811-1823, doi:10.1002/ejoc.201201400 (2013).

9 DePamphilis, B. V., Averill, B. A., Herskovitz, T., Que, L. & Holm, R. H. Synthetic analogs of the active sites of iron-sulfur proteins. VI. Spectral and redox characteristics of the tetranuclear clusters $[Fe_4S_4(SR)_4]^{2-}$. *J. Am. Chem. Soc.* **96**, 4159-4167, doi:10.1021/ja00820a017 (1974).

10 Ngo, K. T. *et al.* Turning on the Protonation-First Pathway for Electrocatalytic CO_2 Reduction by Manganese Bipyridyl Tricarbonyl Complexes. *J. Am. Chem. Soc.* **139**, 2604-2618, doi:10.1021/jacs.6b08776 (2017).

11 Sampson, M. D. & Kubiak, C. P. Manganese Electrocatalysts with Bulky Bipyridine Ligands: Utilizing Lewis Acids To Promote Carbon Dioxide Reduction at Low Overpotentials. *J. Am. Chem. Soc.* **138**, 1386-1393, doi:10.1021/jacs.5b12215 (2016).

12 Waldie, K. M., Ostericher, A. L., Reineke, M. H., Sasayama, A. F. & Kubiak, C. P. Hydricity of Transition-Metal Hydrides: Thermodynamic Considerations for CO_2 Reduction. *ACS Catal.* **8**, 1313-1324, doi:10.1021/acscatal.7b03396 (2018).

13 Fogeron, T. *et al.* A Bioinspired Nickel(bis-dithiolene) Complex as a Homogeneous Catalyst for Carbon Dioxide Electroreduction. *ACS Catal.* **8**, 2030-2038, doi:10.1021/acscatal.7b03383 (2018).

14 Lam, Y. C., Nielsen, R. J., Gray, H. B. & Goddard, W. A. A Mn Bipyrimidine Catalyst Predicted To Reduce CO_2 at Lower Overpotential. *ACS Catal.* **5**, 2521-2528, doi:10.1021/cs501963v (2015).

15 Stirling, M. J., Sweeney, G., MacRory, K., Blacker, A. J. & Page, M. I. The kinetics and mechanism of the organo-iridium-catalysed enantioselective reduction of imines. *Org. Biomol. Chem.* **14**, 3614-3622, doi:10.1039/C6OB00245E (2016).

16 Costentin, C., Drouet, S., Robert, M. & Savéant, J.-M. A Local Proton Source Enhances CO_2 Electroreduction to CO by a Molecular Fe Catalyst. *Science* **338**, 90, doi:10.1126/science.1224581 (2012).

17 Roy, S. *et al.* Molecular Cobalt Complexes with Pendant Amines for Selective Electrocatalytic Reduction of Carbon Dioxide to Formic Acid. *J. Am. Chem. Soc.* **139**, 3685-3696, doi:10.1021/jacs.6b11474 (2017).

18 Dey, S., Todorova, T. K., Fontecave, M. & Mougel, V. Electroreduction of CO_2 to Formate with Low Overpotential using Cobalt Pyridine Thiolate Complexes. *Angew. Chem. Int. Ed.* **59**, 15726-15733, doi:10.1002/anie.202006269 (2020).

19 Chen, L. *et al.* Molecular Catalysis of the Electrochemical and Photochemical Reduction of CO_2 with Earth-Abundant Metal Complexes. Selective Production of CO vs HCOOH by Switching of the Metal Center. *J. Am. Chem. Soc.* **137**, 10918-10921, doi:10.1021/jacs.5b06535 (2015).

20 Bi, J., Hou, P., Liu, F.-W. & Kang, P. Electrocatalytic Reduction of CO_2 to Methanol by Iron Tetradentate Phosphine Complex Through Amidation Strategy. *ChemSusChem* **12**, 2195-2201, doi:10.1002/cssc.201802929 (2019).

21 Taheri, A., Carr, C. R. & Berben, L. A. Electrochemical Methods for Assessing Kinetic Factors in the Reduction of CO_2 to Formate: Implications for Improving Electrocatalyst Design. *ACS Catal.* **8**, 5787-5793, doi:10.1021/acscatal.8b01799 (2018).

22 Liu, F.-W., Bi, J., Sun, Y., Luo, S. & Kang, P. Cobalt Complex with Redox-Active Imino Bipyridyl Ligand for Electrocatalytic Reduction of Carbon Dioxide to Formate. *ChemSusChem* **11**, 1656-1663, doi:10.1002/cssc.201800136 (2018).

23 Kang, P. *et al.* Selective Electrocatalytic Reduction of CO_2 to Formate by Water-Stable Iridium Dihydride Pincer Complexes. *J. Am. Chem. Soc.* **134**, 5500-5503, doi:10.1021/ja300543s (2012).

24 Ceballos, B. M. & Yang, J. Y. Directing the reactivity of metal hydrides for selective CO_2 reduction. *Proc. Nat. Acad. Sci.* **115**, 12686, doi:10.1073/pnas.1811396115 (2018).

25 Machan, C. W. *et al.* Electrocatalytic Reduction of Carbon Dioxide by Mn(CN)(2,2′-bipyridine)$(CO)_3$: CN Coordination Alters Mechanism. *Inorg. Chem.* **54**, 8849-8856, doi:10.1021/acs.inorgchem.5b01715 (2015).

26 Wang, X. *et al.* Site-isolated manganese carbonyl on bipyridine-functionalities of periodic mesoporous organosilicas: efficient CO_2 photoreduction and detection of key reaction intermediates. *Chem. Sci.* **8**, 8204-8213, doi:10.1039/C7SC03512H (2017).

27 Machan, C. W., Sampson, M. D., Chabolla, S. A., Dang, T. & Kubiak, C. P. Developing a Mechanistic Understanding of Molecular Electrocatalysts for CO_2 Reduction using Infrared Spectroelectrochemistry. *Organometallics* **33**, 4550-4559, doi:10.1021/om500044a (2014).

28 Rønne, M. H. *et al.* Ligand-Controlled Product Selectivity in Electrochemical Carbon Dioxide Reduction Using Manganese Bipyridine Catalysts. *J. Am. Chem. Soc.* **142**, 4265-4275, doi:10.1021/jacs.9b11806 (2020).

29 Franco, F. *et al.* Local Proton Source in Electrocatalytic CO_2 Reduction with [Mn(bpy–R)$(CO)_3$Br] Complexes. *Chem. Eur. J.* **23**, 4782-4793, doi:10.1002/chem.201605546 (2017).

30 Cotton, F. A., Down, J. L. & Wilkinson, G. 167. Infrared spectra of manganese carbonyl hydride and deuteride. *J. Chem. Soc.*, 833-837, doi:10.1039/JR9590000833 (1959).

31 Sampson, M. D. *et al.* Manganese Catalysts with Bulky Bipyridine Ligands for the Electrocatalytic Reduction of Carbon Dioxide: Eliminating Dimerization and Altering Catalysis. *J. Am. Chem. Soc.* **136**, 5460-5471, doi:10.1021/ja501252f (2014).

32 Sampson, M. D. *et al.* Direct observation of the reduction of carbon dioxide by rhenium bipyridine catalysts. *Energy Environ. Sci.* **6**, 3748-3755, doi:10.1039/C3EE42186D (2013).

33 Chen, Z. *et al.* Electrocatalytic reduction of CO_2 to CO by polypyridyl ruthenium complexes. *Chem. Commun.* **47**, 12607-12609, doi:10.1039/C1CC15071E (2011).

34 in *Overview of Reference Electrodes and Alternative Reference Electrodes DRK10053 (REV001 |APR 2016)* https://pineresearch.com/shop/wp-content/uploads/sites/2/2016/2010/DRK10053-Overview-of-Reference-Electrode-Operation-and-Alternative-Reference-Electrodes-REV10001.pdf (Pine Research, 2016).

35 Reynolds, J. G., Laskowski, E. J. & Holm, R. H. Proton magnetic resonance properties of the tetranuclear clusters $[Fe_4S_4(SR)_4]^{3-}$, analogs of the 4-Fe sites of reduced ferredoxins. *J. Am. Chem. Soc.* **100**, 5315-5322, doi:10.1021/ja00485a012 (1978).

36 Bhattacharya, M., Sebghati, S., VanderLinden, R. T. & Saouma, C. T. Toward Combined Carbon Capture and Recycling: Addition of an Amine Alters Product Selectivity from CO to Formic Acid in Manganese Catalyzed Reduction of CO_2. *J. Am. Chem. Soc.* **142**, 17589-17597, doi:10.1021/jacs.0c07763 (2020).

37 Savéant, J.-M. a. C., C. in *Elements of Molecular and Biomolecular Electrochemistry* 81-181 (2019).

38 Wise, C. F., Agarwal, R. G. & Mayer, J. M. Determining Proton-Coupled Standard Potentials and X–H Bond Dissociation Free Energies in Nonaqueous Solvents Using Open-Circuit Potential Measurements. *J. Am. Chem. Soc.* **142**, 10681-10691, doi:10.1021/jacs.0c01032 (2020).

39 Warren, J. J., Tronic, T. A. & Mayer, J. M. Thermochemistry of Proton-Coupled Electron Transfer Reagents and its Implications. *Chem. Rev.* **110**, 6961-7001, doi:10.1021/cr100085k (2010).

40 Madsen, M. R. *et al.* Promoting Selective Generation of Formic Acid from CO_2 Using $Mn(bpy)(CO)_3Br$ as Electrocatalyst and Triethylamine/Isopropanol as Additives. *J. Am. Chem. Soc.* **143**, 20491-20500, doi:10.1021/jacs.1c10805 (2021).

41 Huynh, M. T., Anson, C. W., Cavell, A. C., Stahl, S. S. & Hammes-Schiffer, S. Quinone 1 e^- and 2 e^-/2 H^+ Reduction Potentials: Identification and Analysis of Deviations from Systematic Scaling Relationships. *J. Am. Chem. Soc.* **138**, 15903-15910, doi:10.1021/jacs.6b05797 (2016).

42 Berning, D. E., Noll, B. C. & DuBois, D. L. Relative Hydride, Proton, and Hydrogen Atom Transfer Abilities of $[HM(diphosphine)_2]PF_6$ Complexes (M = Pt, Ni). *J. Am. Chem. Soc.* **121**, 11432-11447, doi:10.1021/ja991888y (1999).